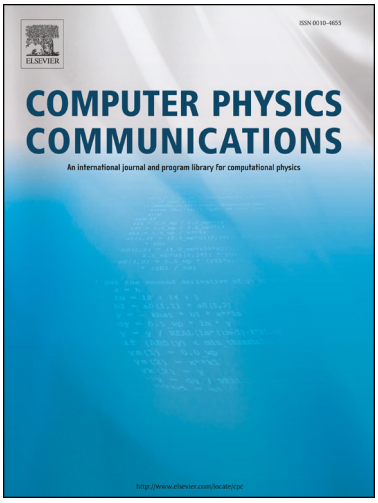

3D Ray Tracing Solver for Communication Blackout Analysis in Atmospheric Entry Missions

Vincent F. Giangaspero, Vatsalya Sharma, Johannes Laur, Jan Thoemel, Alessandro Munafò et al.

PII: S0010-4655(23)00008-5
DOI: https://doi.org/10.1016/j.cpc.2023.108663
Reference: COMPHY 108663

To appear in: *Computer Physics Communications*

Received date: 3 October 2022
Revised date: 19 December 2022
Accepted date: 5 January 2023

Please cite this article as: V.F. Giangaspero, V. Sharma, J. Laur et al., 3D Ray Tracing Solver for Communication Blackout Analysis in Atmospheric Entry Missions, *Computer Physics Communications*, 108663, doi: https://doi.org/10.1016/j.cpc.2023.108663.

3D Ray Tracing Solver for Communication Blackout Analysis in Atmospheric Entry Missions

Vincent F. Giangaspero[a,b,*], Vatsalya Sharma[b], Johannes Laur[d], Jan Thoemel[d], Alessandro Munafò[c], Andrea Lani[a,b], Stefaan Poedts[b,e]

[a] *Von Karman Institute for Fluid Dynamics, Waterloosesteenweg 72, 1640, Sint-Genesius-Rode, Belgium*
[b] *Centre for Mathematical Plasma-Astrophysics, KU Leuven, Celestijnenlaan 200B, B-3001 Leuven, Belgium*
[c] *Department of Aerospace Engineering, Talbot Laboratory, 104 S. Wright St., Urbana, IL 61801, United States of America*
[d] *University of Luxembourg, Avenue J.F. Kennedy 29, L-1855, Luxembourg*
[e] *Institute of Physics, University of Maria Curie-Skłodowska, ul. Radziszewskiego 10, PL-20-031 Lublin, Poland*

Abstract

During the atmospheric entry phase at hypersonic speed, the radio communication from/to a space vehicle can be disrupted due to the formation of a plasma sheath within the surrounding flow field. In order to characterize such communication blackout phases, this work presents a numerical methodology combining Computational Fluid Dynamic (CFD) simulations of ionized chemically reacting entry flows by means of Computational Object-Oriented Libraries for Fluid Dynamics (COOLFluiD) and a ray tracing analysis by means of the newly developed BlackOut RAy Tracer (BORAT). The latter is based on the numerical solution of the 3D Eikonal system of equations, offering a fast, efficient and accurate method to analyse the interaction between electromagnetic signals and weakly ionised plasmas. The proposed methodology, and BORAT in particular, is first verified on popular benchmark cases and then used to analyse the European Space Agency (ESA) 2016 ExoMars Schiaparelli entry flight into Martian environment. The corresponding results demonstrate the validity of the proposed ray tracing approach for predicting communication blackout, where signals emitted from the on-board antenna undergo reflection and refraction from the plasma surrounding the entry vehicle, and the advantage of a 3D approach for analysing real flight configuration.

Keywords: Numerical algorithms, Computational Fluid Dynamics, plasma flows, communication blackout, hypersonic flows, ray tracing

1. Introduction

Atmospheric (re)-entry is one of the most challenging phases and one of the most critical aspects to consider for the design of a successful space mission. Spacecraft flying at hypersonic speeds undergo large pressure and thermal loads, which, if not properly quantified, may compromise structural integrity and result in mission failure [1]. Furthermore, communication systems are disrupted during this delicate phase, ultimately compromising data transmission and control [2]. Since the early days of the space era, communication blackout has been an open challenge and no definitive solutions have been developed so far in order to ensure its mitigation. Developing strategies to ensure propagation of radio signals from/to ground control is of paramount importance for the success of a space mission. The reduction of the overall communication blackout period would limit data transmission losses and therefore lead to safer control during entry. This is one of the key challenges to be tackled, for future manned or unmanned space exploration missions, space tourism or military applications that will all require telecommunications improvements and safety during flight at hypersonic speeds. The current aerospace technology requires further investigations and

*Corresponding author
Email addresses: vincent.giangaspero@kuleuven.be (Vincent F. Giangaspero), vatsalya.sharma@kuleuven.be (Vatsalya Sharma), johannes.laur@uni.lu (Johannes Laur), jan.thoemel@uni.lu (Jan Thoemel), munafo@illinois.edu (Alessandro Munafò), andrea.lani@kuleuven.be (Andrea Lani), stefaan.poedts@kuleuven.be (Stefaan Poedts)

investments to overcome this issue, especially considering the recent renewed interest in future human missions to colonize space and, in particular, Mars. As of today, spacecraft solely rely on satellite constellations to communicate through the plasma wake, partially reducing the telecommunication blackout period, but no active system to tackle this issue has been successfully integrated into space vehicles for operating flights.

The investigation of possible mitigation solutions to the blackout problem requires advanced theoretical, experimental and numerical investigation of the involved phenomena, which are all part of ongoing research efforts. Experiments, particularly ground testing, play a vital role in design and development of space vehicles, but any available experimental facility can only partially reproduce the conditions that are experienced during a full hypersonic re-entry flight, and with associated high costs. The most cost-effective option to consider to reproduce all relevant flow-related phenomena which are involved during a hypersonic re-entry is Computational Fluid Dynamics (CFD) in combination with possibly other numerical models, e.g. to simulate thermal shielding materials or electromagnetic fields. The use of CFD is particularly insightful for the early design stages of future space technologies, allowing for the investigation of different solutions and their effectiveness, before embarking in expensive and time-consuming on-ground and, ideally, flight experiments. In addition, in the case of radio communication blackout, the experimental characterization of realistic flight conditions is very challenging (if not impossible) in ground facilities, considering the combination of extreme physical phenomena such as high-speed flows and high-frequency transmission systems. For instance, reflections of radio signals on the walls of the testing chamber and the difficulties to simulate the same exact plasma field configuration and properties (e.g. shape, electron density distribution) around the miniaturized vehicle model. This kind of experiments can be used to verify some plasma modelling aspects (e.g. the electrical conductivity, the chemical reactions rates), to estimate the mitigation of attenuation of signal in specific directions and help validating the numerical tools/simulations for simplified testable scenarios. Thus, numerical models that can simulate hypersonic flows and high transmission frequencies systems, by including all the relevant effects corresponding to the real flight conditions, are of paramount importance for the development of new technologies. To this end, this work is part of research efforts aiming at developing more accurate and efficient numerical tools to better characterize, predict and investigate solutions to the communication blackout problem.

Within this context, the tools developed in this work are part of the Magnetohydrodynamic Enhanced Entry System for Space Transportation (MEESST) project, featuring an international consortium comprising universities, research institutions and SMEs with multi-disciplinary expertise ranging from plasma/flow/radiation modeling, radio communication, high-temperature superconducting materials, magnet design and cryogenic systems. The project is funded by the Future and Emerging Technologies (FET) program of the European Commission's Horizon 2020 scheme (grant no. 899298). The MEESST project aims at developing a prototype device, utilizing superconducting electromagnets to actively control the plasma surrounding a spacecraft undergoing atmospheric entry [3]. The primary aims of the project are two: to mitigate the Radio Frequency (RF) blackout phenomenon and reduce the heat flux generation on spacecraft's bodies, reducing the need for heavy Thermal Protection Systems (TPS). The Centre for mathematical Plasma-Astrophysics (CmPa) of the University of KU Leuven, coordinator and principal investigator of the MEESST project, leads the research effort in developing and improving numerical models for the atmospheric entry phases.

This paper presents a methodology relying upon CFD simulations and ray tracing techniques in order to analyze and predict communication blackout. Particular focus is given to the development of a novel 3D ray tracing solver called Black-Out-RAy-Tracer (BORAT). The target test-case for the present work is the entry of the 2016 ESA ExoMars mission lander, which experienced 60 seconds of blackout [4]. This mission consisted in the launch of the ExoMars Trace Gas Orbiter (TGO), an atmospheric research orbiter, and the deployment of Schiaparelli, the Entry, Descent, and Landing Demonstrator Module (EDM). The objective of the landing mission was to assess and validate ESA's technologies capabilities in preparation of future missions [5]. 2D axial-symmetric hypersonic CFD simulations are performed over the ExoMars Schiaparelli module at different trajectory points with the COOLFluiD aerothermodynamics Finite Volume solver coupled with the PLATO thermochemistry library. The axial-symmetric CFD solutions are then extruded and rotated to generate a 3D flow solution, that is used as an input for the ray tracing solver. The latter is implemented in the Matlab software code BORAT, of which version 3.0 has been developed for 3D simulations (https://github.com/JanThoemel/borat). BORAT uses the vehicle geometry, the plasma field surrounding the spacecraft (as computed by non-equilibrium hypersonic CFD simulations) plus antenna characteristics and location as inputs. The propagation of the electromagnetic (EM) waves radiated by the on-board antenna is modelled using a ray tracing "shooting-and-bouncing" technique through the non-uniform plasma region around the vehicle until such signals escape from the plasma region.

This paper aims at introducing the BORAT code and demonstrating its ability to accurately predict and characterize the blackout phases of a real space mission in terms of duration and wave interaction with the plasma flow surrounding the spacecraft. BORAT provides useful and accurate numerical results along with a very flexible blackout prediction tool that is potentially capable of assisting system engineers in the development of next generation solutions for continuous communication during atmospheric entries.

The manuscript is structured as follows. Section 2 recalls the main concepts related to communication blackout during atmospheric entry. The numerical modeling, including CFD solver and plasma optical models, are described in Sec. 3. The implementation and development of the ray tracing solver is detailed in Sec. 4. Results are presented and discussed in Sec. 5. Finally, conclusions are given in Sec. 6.

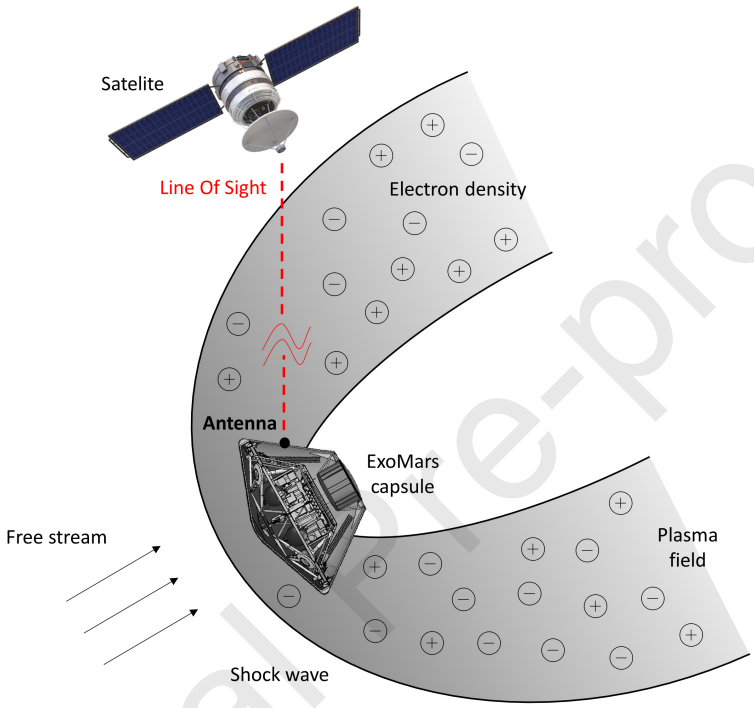

Figure 1: Radio frequency blackout for flow over entry capsule.

2. Communication blackout

During the entry phase, spacecraft enter a planetary atmosphere at hypersonic speed, typically around 6-10 $km\ s^{-1}$, generating strong shock waves and large aerodynamic heating [6]. When the temperature is high enough to excite the gas molecule internal energy modes up to the point where dissociation and ionization reactions occur, a plasma sheath is generated around the vehicle. Plasma interacts with the EM signals from/to the vehicle, disrupting the functionality of the on-board signal transmission systems [7]. The resulting plasma layer usually has an electron number density of 10^{17} to 10^{20} m^{-3} [8]. The amount of electrons generated in the plasma field characterizes the ionization level which in communication problems is quantified by the plasma natural resonant frequency. For a given electron number density N_e, the plasma frequency has a square root dependence on the electron number density $f_p \sim \sqrt{N_e}$. Plasma attenuates the radio frequency (RF) signal which is used for communication when the transmission frequency is comparable to the plasma frequency [9]. At each transmission frequency corresponds a critical electron density $N_{e_{crit}}$ that, if generated in the entry plasma layer, results in blackout conditions. Figure 1 shows a sketch representation of the radio communication blackout for an atmospheric entry capsule. At the beginning of an entry flight, electron production is generally low due to the low density of the atmosphere. As the capsule flies at higher speeds through denser atmospheric layers, electron production increases, reaching a maximum and generating the higher blackout

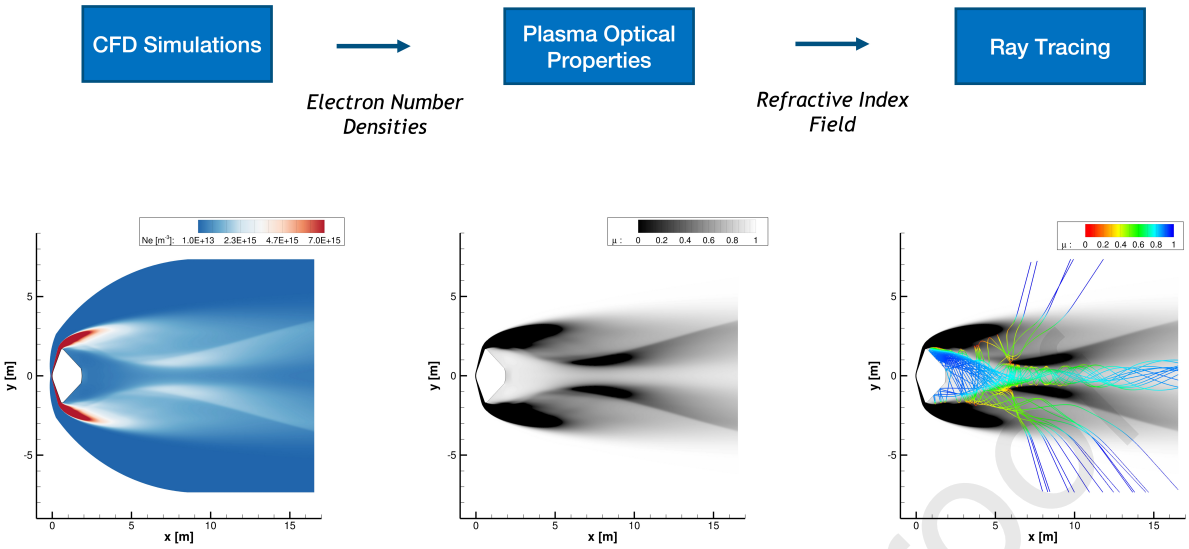

Figure 2: Radio frequency blackout analysis methodology: from CFD simulations to ray tracing analysis.

conditions. After this phase, the electron production diminishes due to the lower speed of the capsule during the final landing phase. In general higher ionisation levels occur in the front part of the vehicle, in the proximity of the stagnation zone. For this reason, entry capsules usually place their antenna in the backshell of the vehicle. However, at the peak of communication blackout, the plasma region propagates considerably in the wake, disrupting the signal propagation also in this region [10].

3. Radio blackout analysis methodology

Numerical analysis of communication blackout involves two different steps: first the calculation of electron density profiles from CFD simulations; second the modeling of the RF signal propagation through plasma. These two phenomena are characterised by two distinct time scales: the plasma variation in time during an entry trajectory can be considered evolving following the velocity of the spacecraft through the atmosphere during its planetary descent, typically around 6-10 $km\ s^{-1}$. RF signal propagation in the entry plasma is characterised by propagation velocities in the range of speed of light, with an order of magnitude of $10^5\ km\ s^{-1}$. Thus, considering the great differences in the time scales of these phenomena [11], the plasma variation in time during an entry trajectory can be considered slow with respect to the RF signal propagation. This allows for analysing entry communication blackout by simulating different flow field conditions, in which plasma is considered constant while solving the wave propagation in its interior. The hypersonic flow generated around the space vehicle is computed by solving the Navier-Stokes equations with different thermo-chemical models depending on the entry conditions.

To analyze the propagation of EM waves in plasma, the modeling strategies are generally divided in full wave methods and ray tracing methods. Full wave methods, i.e. FDTD,FEM [12], solve the full set of Maxwell equations without approximations, with the drawback of large computational cost. This makes their use particularly disadvantageous for large propagation problems, such as in space entry applications, where plasma is generated in the front part the spacecraft but also largely affects the flow in the wake region downstream, the main region of propagation of communication signal. For this reason, the use of ray tracing methods is particularly indicated to analyze large propagation problems, since they are based on approximate solutions of Maxwell equations, reducing the complexity of the corresponding numerical simulation. Reference works regarding Earth re-entry missions are Ramjatan et al [13], who performed CFD simulations of small cone-shaped re-entry vehicles, and Takahashi et al. [14] who examined the blackout of ESA's Atmospheric Re-entry Demonstrator (ARD). The first example of application of ray tracing theory to atmospheric entry problem is the work of Vecchi et al. [15]. For Mars entry missions, very limited work has been published, where the Line Of Sight (LOS) approach was mainly used [16]. This simple technique is based on the

comparison between the maximum and critical electron number density along the LOS between the spacecraft and the receiving satellite. The main limitation of this approach is the lack of multidimensional information on the interaction between the RF signal and the plasma. Moreover, the use of highly advanced methods allows for reproducing more complex waves phenomena such as reflection, refraction and phase modulation. A preliminary application of ray tracing methods to analyse blackout in Martian atmosphere is the work of Ramjatan et al [17], in which a a simplified hybrid CFD/Lagrangian approach (i.e. extrapolating corresponding electron densities with a Lagrangian solver from 2D axial-symmetric CFD solutions for neutral gas mixtures) has been coupled to a rather basic ray tracing algorithm in order to asses the validity of the proposed analysis model. This approach has been further developed in [18] by the use of an extended version of the same CFD solver, for neutral and ionized flows, capable of computing ionization levels in the whole computational domain, with a particular focus on the extended wake region. In this work, the previous methodology is enhanced first by the implementation of a more sophisticated, accurate and efficient ray tracing algorithm, the Eikonal set of equations. Second, the BORAT code for analysing/predicting blackout has been upgraded to a 3D formulation, using the new Eikonal formulation, in order to deliver a tool capable of reproducing real flight configurations. Another important difference concerns the way the input electron number density field is generated: while in the [17] it was extrapolated with a rather cumbersome (and not fully automatic) approach using a lagrangian solver (LARSEN) from a CFD solution in chemical nonequilibrium using only neutral species, in this work it is computed directly by the CFD solver using a chemical nonequilibrium model including electrons (and ions) as individual species. The numerical strategy for the communication blackout analysis of this paper is displayed in Figure 2 and consists of:

1. hypersonic *CFD simulations* at different free stream conditions in order to reproduce atmospheric entry trajectories;

2. computing the *optical properties* of plasma by solving the Appleton-Hartree equation for the specific plasma model;

3. application of *ray tracing* for propagating the EM waves through plasma.

This methodology is implemented in the BORAT code. The latter can be easily interfaced to arbitrary hypersonic/entry flow solvers, from which the CFD solutions are used as an input for the ray tracing analysis. Figure 3 shows a flowchart of the BORAT solver and its main constitutive parts. BORAT solver imports mesh and plasma characteristics (i.e. electron densities) from the CFD solution files. Then the plasma optical properties are computed by solving the Appleton-Hartree equation throughout the computational domain. Finally, ray tracing simulations are run to analyse the interaction between EM waves and entry plasma. The ray tracing technique used in this work belongs to the family of *shooting and bouncing* ray tracing (SBR) technique [19], in which rays are emitted from the antenna location and integrated in the numerical domain until they emerge from the plasma. The first version of BORAT (BORAT v1.0) is based on the use of the Snell's law equation and can only be used to analyze radio waves propagation through entry (i.e., weakly ionized) plasmas for 2D configurations. This solver has the capability of analyze radio waves propagation through atmospheric entry, i.e., weakly ionized, plasmas for 2-dimensional situations employing a Snell's law ray tracing algorithm [17, 18]. The Snell's law is the governing equation of geometrical optics, and is the most simplified model for EM waves propagation in a medium. In the context of this paper, BORAT has been extended and upgraded, including the development of a more advanced ray tracing algorithm based on the Eikonal approximation and the development of a 3D version of the code. In the following sections more details will be given on the specific methods developed and employed.

3.1. CFD plasma model

The hypersonic flow which is generated around the entry vehicle is computed by solving the Navier-Stokes equations. The numerical simulations are performed with the Finite Volume (FV) aerothermodynamic solver implemented within the COOLFluiD platform [20, 21]. COOLFluiD (https://github.com/andrealani/COOLFluiD) is a worldclass open source CFD platform for simulating flows and plasmas, originally developed by the Von Karman Institute in collaboration with the CmPA at KU Leuven [22]. It includes multiple 2D and 3D parallel solvers with different numerical methods and physical models. In particular the FV solver for thermochemical non-equilibrium flows has been used in this work. A variant of AUSM+ scheme and limited Least Square solution reconstruction algorithms are

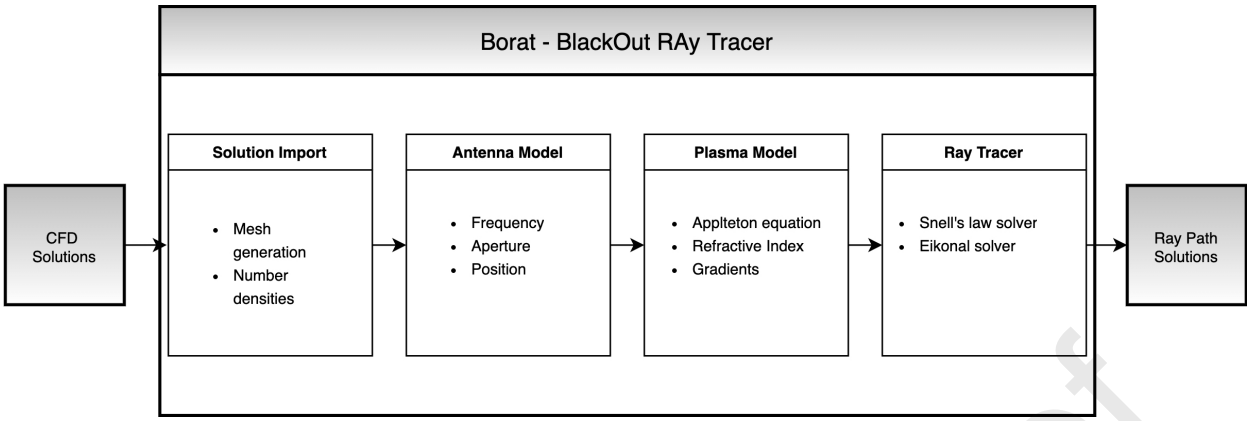

Figure 3: Flowchart of BORAT Ray Tracing code.

used to discretize the convective fluxes for the multi-species and chemically reacting fluid. A fully implicit Backward Euler method is used for converging to steady state. The resulting discretized linear system is solved by Generalized Minimal RESidual (GMRES) algorithms and Additive Schwarz preconditioner from PETSc [23]. COOLFluiD uses finite-rate chemical kinetics models for modelling non-equilibrium processes and all thermodynamics transport and chemical properties are computed by the interfaced PLAsmas in Thermodynamic nOn-equilibrium (PLATO), a thermochemical library which is used for all the simulation. PLATO has been developed at the University of Illinois at Urbana Champaign (UIUC) [24]. More details on the numerical method and physical models available in PLATO may be found in [25]. Dissociation/recombination and ionization of the gas mixture is treated using an Arrhenius form where the backward rate coefficient is determined using the forward rate and equilibrium constant.The COOLFluiD finite volume (FV) solver has been rigorously validated and verified for several applications relevant to this paper which have already been published in the literature (e.g. in [26, 27, 28, 29].) and therefore have not been presented here.

3.2. Optical plasma model

The flow field solution obtained from the hypersonic CFD simulations contains the information about the plasma ionisation levels, which are used as input for the ray tracing analysis. Ray tracing theory is founded on geometrical optics, and provides a reliable method to estimate the dominant path of energy flow in propagating EM waves. The first step for the application of ray tracing is the computation of the plasma optical properties, defined by the Appleton-Hartree equation. Optical properties are defined by the plasma refractive index, which is the parameter that governs the propagation of EM waves in plasma. The Appleton-Hartree equation was developed independently by several different scientists and has been extensively applied to ionospheric propagation problems [30]. In the context of this work, the fundamental theory behind optical properties follows the description of Davies [31], who derives the Appleton equation based on the Maxwell equations and the conservation of momentum of free electrons. It reads as:

$$n^2 = (\mu - \chi i)^2 \,. \tag{1}$$

In this formulation, plasma is characterized by the complex refractive index n, consisting of a real part, μ, and an imaginary part, χ. The real part μ represents the effect of plasma in waves propagation bending, while the imaginary part χ represents the absorptivity, responsible of attenuation effects on travelling waves. The full equation form reads as follows:

$$n^2 = (\mu - \chi i)^2 = 1 - \frac{X}{1 - Zi - \dfrac{{Y_T}^2}{2\,(1 - X - Zi)} \pm \sqrt{\dfrac{{Y_T}^4}{4\,(1 - X - Zi)^2} + {Y_L}^2}}, \tag{2}$$

with:

$$\begin{aligned} X &= e^2 N_e / \left(\epsilon_0 m \omega^2\right) \\ Y_L &= eB_L / \left(m\omega\right) \\ Y_T &= eB_T / \left(m\omega\right) \\ Z &= \nu/\omega \\ \omega &= 2\pi f, \end{aligned} \tag{3}$$

where e denotes the electron charge, N_e the electron number density, ϵ_0 the vacuum permittivity, m_e the electron mass, ν_{eh} the electron-heavy particle collision frequency, f the communication system transmission frequency, B_L and B_T are longitudinal and transversal magnetic fields. The general form of the Appleton-Hartree equation can be reduced depending on the specific characteristic conditions of the plasma. The first reduced form of the Appleton-Hartree equation is the unmagnetized cold plasma form, in which the effect of magnetic fields is neglected in the computation of the refractive index. This is the general case of atmospheric entry plasma, in which no magnetic fields are applied on the spacecraft and planetary magnetic fields can be neglected. In this case, $B_T = B_L = 0$, leading to:

$$n^2 = (\mu - \chi i)^2 = 1 - \frac{X}{1 - Zi}. \tag{4}$$

Solving this equation for μ and χ leads to:

$$\mu^2 = \frac{1}{2}\left(1 - \frac{X}{1+Z^2}\right) + \frac{1}{2}\sqrt{1 - 2\frac{X}{1+Z^2} + \frac{X^2}{1+Z^2}}, \tag{5}$$

and

$$\chi^2 = -\frac{1}{2}\left(1 - \frac{X}{1+Z^2}\right) + \frac{1}{2}\sqrt{1 - 2\frac{X}{1+Z^2} + \frac{X^2}{1+Z^2}}. \tag{6}$$

The resulting equation becomes a function of X, which is a direct function of the electron number density, and Z, which is a direct function of the collision frequency ν. The effect of neglecting or considering electron collisions in the Appleton equation can lead to two different medium characterizations, non-collisional and collisional plasma.

3.2.1. Non-collisional plasma

The simplest case of the Appleton formula can be retrieved by neglecting the effect of collision between electron and heavy particles, $Z \sim 0$, meaning $\nu \ll f$. It reads as follow:

$$n = \mu = \sqrt{1 - X} = \sqrt{1 - \left(\frac{f_p}{f}\right)^2}, \tag{7}$$

$$f_p = \sqrt{kN_e}, \tag{8}$$

$$k = e^2 / \left(4\pi^2 \epsilon_0 m\right). \tag{9}$$

In this formulation, the refractive index is a real number with values between 0 and 1. The refractive index of the plasma thus becomes a solely a function of the electron plasma frequency f_p and a given transmission frequency f in Hz. For a given wave frequency f, the refractive index decreases with an increase of electron density N_e, and for a given electron density the refractive index increases with an increase of wave frequency. Figure 4 describes the distinctive flow structure within the wake flow of an entry capsule and its refractive index field. The front part of the flow is characterized by the presence of an hypersonic thin shock layer, which produces flow ionization. This zone

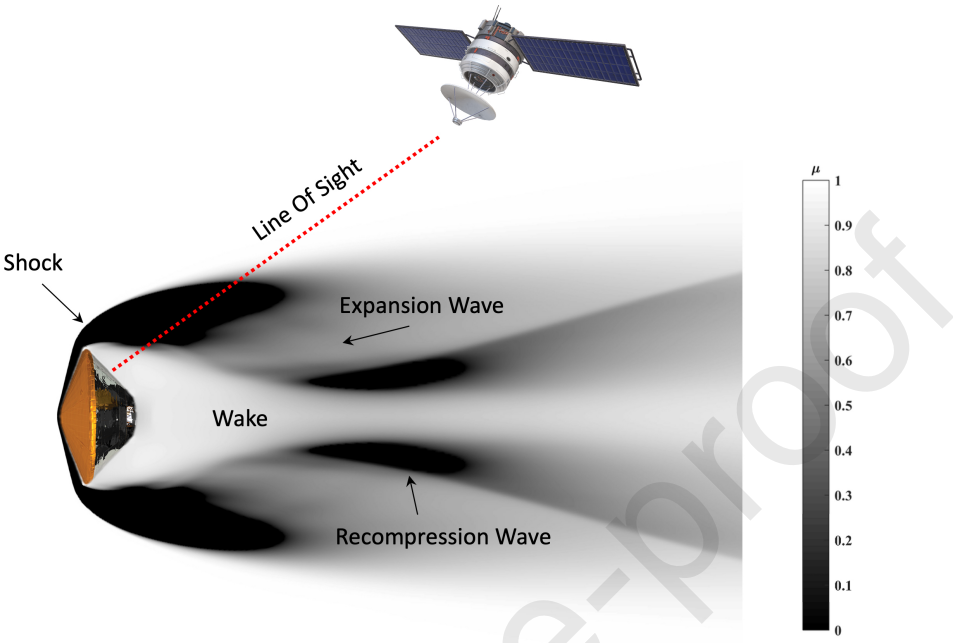

Figure 4: Wake flow structure with refractive index μ over entry capsule

presents the highest values of electron densities, making communications impossible in this direction, with an overall refractive index equal to 0 in the whole front shock layer. The flow is then turned around the shoulder of the vehicle resulting in an expansion fan, which curves the bow shock, decrease the temperature and accelerates the flow. In this region, due to lower temperature values, recombination occurs, reducing the presence of free electrons, as visible from higher values of the refractive index. The expansion region is followed by a recompression shock, that is created as the flow realigns in the wake. The occurrence of different flow features significantly changes the optical properties of the gas, leading to refractive index around unity in colder regions, and to refractive index approaching zero values where ionization levels are higher. Thus, as the EM wave penetrates into levels of increasing electron concentration, μ becomes lower and lower. As demonstrated in previous works [17, 18], the simplification of non-collisional medium is a good approximation to describe the leading phenomena involving blackout during both Earth and Mars atmospheric (re-)entry. Collisional effects can be neglected since high collisional frequency zones are located in the stagnation region of the spacecraft, while EM waves propagate in the wake region, which is typically characterized by lower ionization levels. In these conditions, EM are mainly affected by the presence of plasma and deviates due to the real part of the refractive index.

3.2.2. Collisional plasma

Taking into account the collisional frequency between electrons and heavy particles, equation 4 yields to a complex refractive index n, with non-zero values of the absorptivity coefficient. In this case the collisional frequency has an effect on the absorption of the transmitted signal, but it has also an effect on the real part of the refractive index. Figure 5 shows the dispersion curve, that shows the variation of the real part of the refractive index μ with X for different collision frequencies Z. The line Z=0 represent a non-collisional medium, in which increasing the X value (thus increasing the ratio between electron number densities and transmission frequency), decreases the refractive index μ. By increasing the value of Z we see a deviation from the linear refractive index trend and for high values of the collisional frequency, the refractive index doesn't reach zero, but attains a minimum value. In these conditions total

reflection never really occurs.

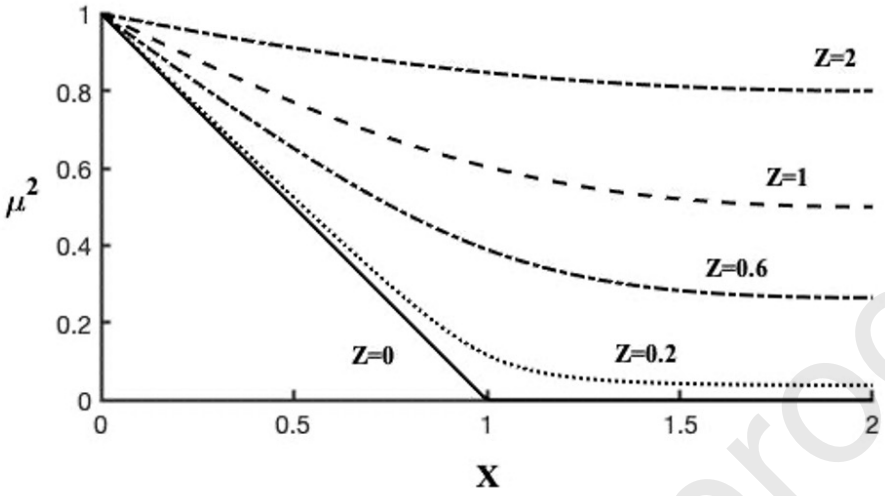

Figure 5: Dispersion curve: deviation of refractive index μ with X for different collisional frequencies.

The absorptivity coefficient represents the exponential decreasing amplitude of a one-dimensional traveling wave [31], and the following quantity:

$$k = \frac{2\pi f}{c}\chi \tag{10}$$

is a measure of the decay of amplitude per unit distance and is called absorption coefficient k (kappa). This formula gives the absorption in nepers per meter, where 1 neper=8.69 dB. By integrating the absorption coefficient along the path of the transmitted signal, is possible to calculate the total attenuation due to absorption by collision with charged particles.

4. BORAT: Black-Out-RAy-Tracer solver

The application of ray tracing techniques to space (re-)entry communication has been proved to be a valid and promising approach to describe the phenomena involving blackout. The ray tracing method results in numerically efficient solvers, in which EM waves wavefronts are discretized with a beam of ray: each ray is independent and uncoupled with respect to the other rays, allowing easy parallelization, with a complexity that scales linearly. To compute the EM waves propagation through the entry plasma, the newly implemented ray tracing algorithm is based on the Eikonal approximation. The Eikonal equation is an approximate solution of Maxwell's equations in the high-frequency range [32]. At large frequencies, electric and magnetic fields may be expressed as:

$$\begin{aligned} E(r) &\simeq E_0 e^{-\imath k_0 S(r)} \\ H(r) &\simeq H_0 e^{-\imath k_0 S(r)}, \end{aligned} \tag{11}$$

where $S(r)$ is the normalised Eikonal phase function, defining the wave-front surface. Inserting the high frequency fields into Maxwell's equations leads to the Eikonal equation:

$$|\nabla S| = \mu, \tag{12}$$

that defines the relation between the direction of propagation of an EM wave and the refractive index of the medium. The equation 12 can be rewritten in characteristic form, with the advantage of a more convenient representation

to retrieve the ray trajectories equations. This may be achieved by introducing the normalized local wave vector $\xi = \nabla S\,\mathrm{K}$, that defines the propagation direction of the EM wave, and the position vector $x_i = (x_1, x_2)$. Using the arc-length s along the ray, one arrives at the following system of ordinary differential equations:

$$\begin{aligned} \frac{\partial x_i}{\partial s} &= \frac{\xi_i}{\mu}, \\ \frac{\partial \xi_i}{\partial s} &= \frac{\partial \mu}{\partial x_i}. \end{aligned} \tag{13}$$

The Eikonal approximation is valid as long as medium properties vary slowly over a length-scale of the order of the signal wavelength [32]. In a hypersonic entry plasma, this assumption can be considered valid in the whole wake region. As visible in Figure 4 strong gradients are mainly located in the front part of the vehicle, a zone non suitable for the propagation of EM waves due to the high ionisation level of the flow. The system 13, along with prescribed initial conditions in terms of position and angle of the emitted ray, allows for predicting ray trajectories and states that the curvature of rays at each point is proportional to the gradient of the refractive index. The validity of characteristic solution of the Eikonal equation, namely the ray trajectories, falls in layers of plasma in which the value of the refractive index μ vanishes. These conditions are generally referred as cut-off conditions, and they are treated as localised reflection conditions. However, these conditions are rarely encountered, since in entry plasma scenarios high-density electron layers with steep variations are generally located in the front part of the vehicle, not designed for communication propagation. The Eikonal formulation presents three main advantages. First of all, the second order continuity in refractive index of the Eikonal formulation allows us to increase the ray tracing solution accuracy with respect to the first order ray tracing Snell's law algorithm. Second, the Ordinary Differential Equations (ODE) system resulting from the Eikonal equation (20) is solved using a Runge-Kutta method (RK4) [33] with adaptive integration step refinement. Last, one of the main advantages of the Eikonal system of equation is the decoupled form of the space variables, allowing algorithmic simplicity that leads to a straightforward development of a 3D version of the solver, as it will be discussed in the next section.

Table 1: Performance comparison between Eikonal solver and Snell's law ray tracing algorithm.

Solver	N steps	Runtime [s]	Speed-up
Eikonal	1141	6.05	x1
Snell's law: s = 0.1	196	91.43	x15
Snell's law: s = 0.05	376	153.32	x25
Snell's law: s = 0.02	877	410.09	x68
Snell's law: s = 0.01	1824	851.45	x140

Figure 6 shows the comparison of a single ray solution between the Eikonal equation solver and the Snell's law marching in space solver, both in terms of trajectory convergence and runtime. Due to the first order dependency on the refractive index variations, the Snell's law solver requires small integration step sizes s to converge to the same ray solution of the Eikonal solver. For this reason, the new Eikonal solver shows a performance increase of over 100x times with respect to the previous marching in space method. Figure 7 summarizes the functionality of the Eikonal ray tracing algorithm. For a 2D formulation, refractive index gradients are reconstructed from the plasma field with a first order approximation:

$$\mu\,(x, y) = \frac{\partial \mu}{\partial x} x + \frac{\partial \mu}{\partial y} y + \mu_0 \tag{14}$$

The refractive index $\mu(x, y)$ is assumed to be a piece-wise planar function over the computational domain. For each computational domain mesh element, the reconstructed gradient is computed by solving the following system of equation:

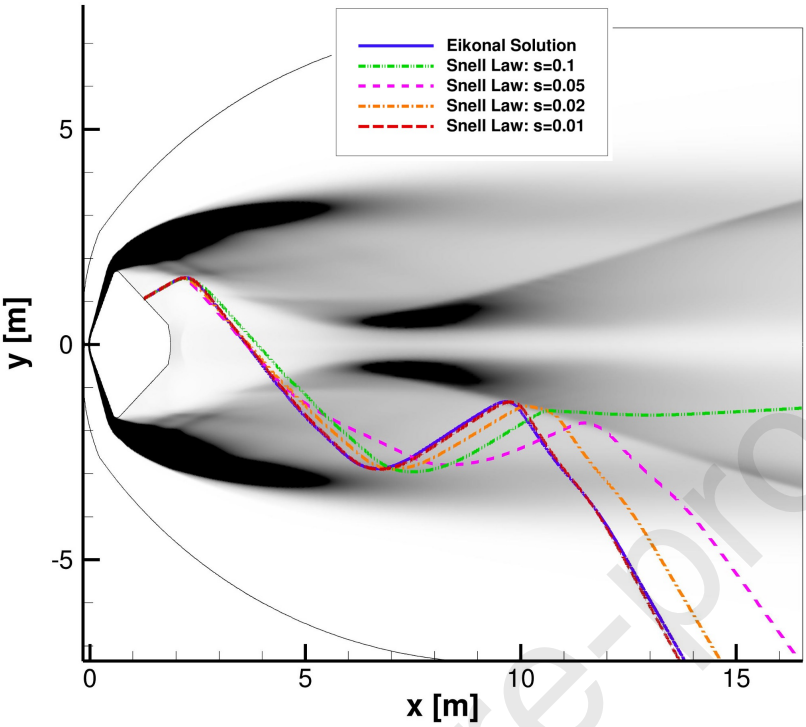

Figure 6: Single ray solution comparison for the different ray tracing algorithms.

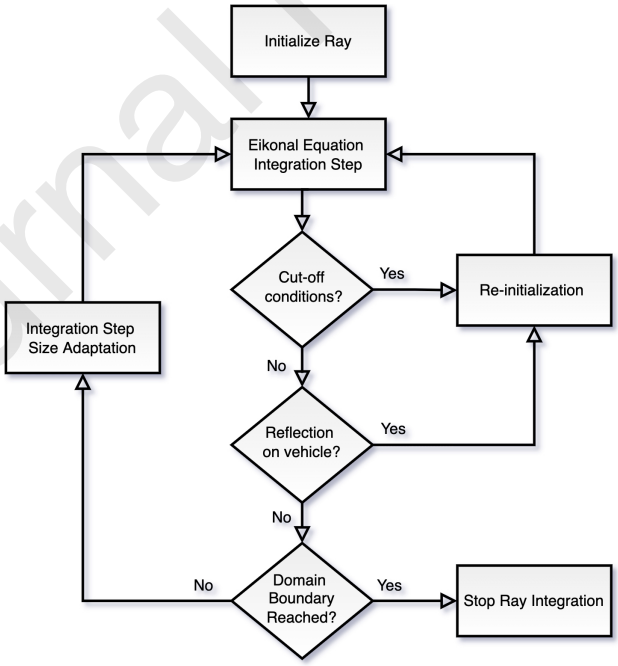

Figure 7: Eikonal ray tracing algorithm

$$\begin{bmatrix} x_1 & y_1 & 1 \\ x_2 & y_2 & 1 \\ x_3 & y_3 & 1 \end{bmatrix} \begin{bmatrix} \frac{\partial \mu}{\partial x} \\ \frac{\partial \mu}{\partial y} \\ \mu(x,y) \end{bmatrix} = \begin{bmatrix} \mu(x_1,y_1) \\ \mu(x_2,y_2) \\ \mu(x_3,y_3) \end{bmatrix} \tag{15}$$

where:

$$\nabla \mu|_T = \begin{bmatrix} \frac{\partial \mu}{\partial x} & \frac{\partial \mu}{\partial y} \end{bmatrix} \tag{16}$$

The partial derivative at each node is the weighted sum of each of the partial derivatives of the triangles associated with that node. The weightings $\omega_i = A_i/A_{tot}$ are the areas of each triangle divided by the total area of all triangles associated with that node.

$$\nabla \mu|_n = \sum_{i=1}^{k} \omega_i \nabla \mu|_{T_i} \tag{17}$$

Figure 8 shows the good agreement achieved with this method between the analytical and the numerical gradient computed for a reference refractive index field. The implemented 2D ray trajectories Eikonal have been verified against two reference optical systems, as shown in figure 9.

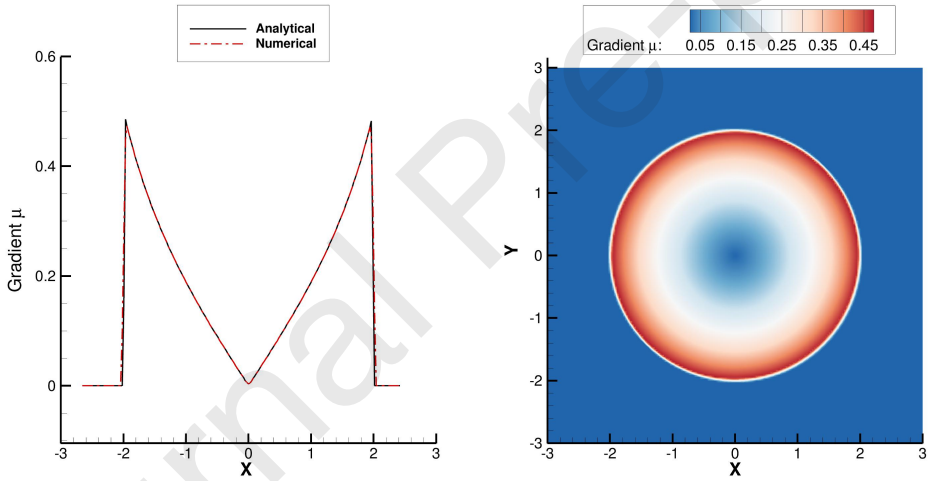

Figure 8: Comparison of refractive index gradient: numerical vs analytical at $Y = 0$.

The first verification case is related to the correct description of the trajectory in the Luneburg lens optical system [34], a spherical symmetric gradient index lens with refractive index given by:

$$\mu = \sqrt{2 - \left(\frac{r}{R}\right)^2} \tag{18}$$

where R is the radius of the lens. This lens has the characteristic of focusing and incident planar wave on the opposite pole. Conversely, waves produced by a source located on the surface of the lens are collimated such that a plane wave front results at the opposite side. The second verification case is the "Maxwell fisheye" lens [35], with a refractive index as:

$$\mu = \frac{2}{1 + \left(\frac{r}{R}\right)^2} \tag{19}$$

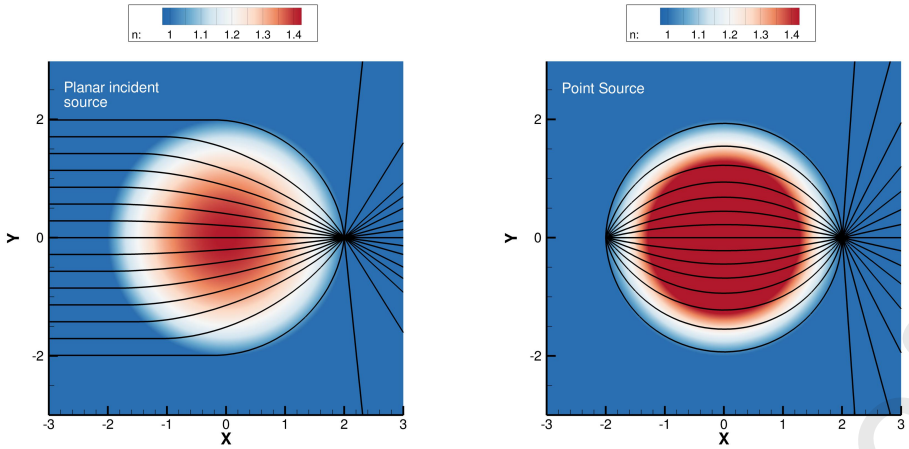

Figure 9: Eikonal two-dimensional solver trajectory verification: Luneburg lens (left) and Maxwell fisheye (right).

This lens has a refractive index constant equal to 1 at its radius, and has the property that rays crossing the lens are redirected to the antipodal point of intersection. In figure 9, the ray source has been positioned at the edge of the lens, and it is possible to observe how all the rays are redirected to the antipodal source point.

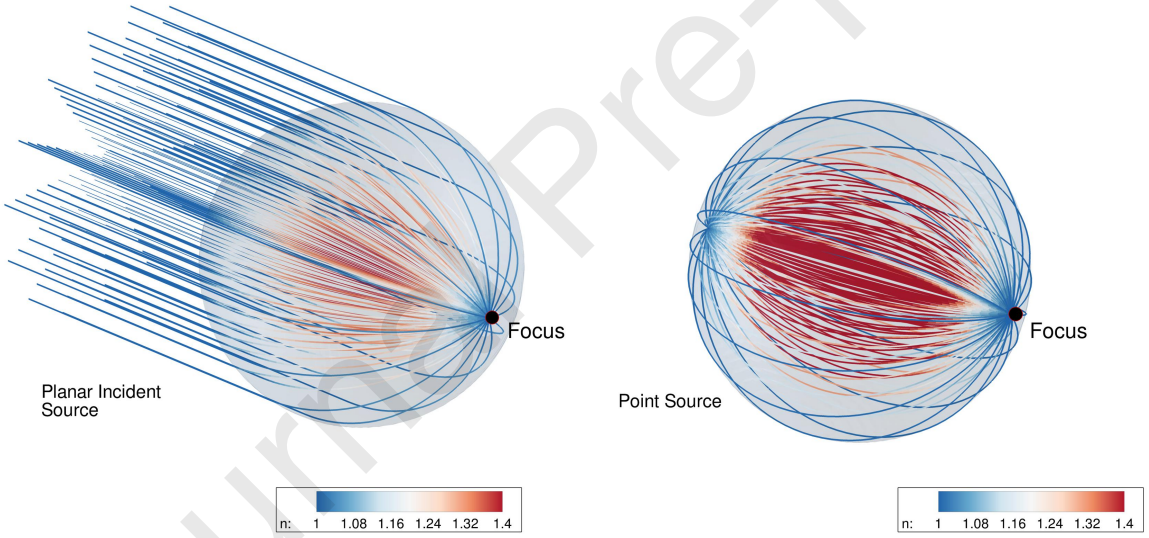

Figure 10: Eikonal 3D solver trajectory verification: Luneburg lens (left) and Maxwell fisheye (right)

4.1. BORAT 3.0 - 3D ray tracing

Following the implementation of the two-dimensional version of the Eikonal solver, the next step has been the development of its 3D version, whose system of equations reads as follows:

$$\begin{aligned} \frac{\partial x}{\partial s} &= \frac{\xi_1}{n}, & \frac{\partial \xi_1}{\partial s} &= \frac{\partial n}{\partial x} \\ \frac{\partial y}{\partial s} &= \frac{\xi_2}{n}, & \frac{\partial \xi_2}{\partial s} &= \frac{\partial n}{\partial y} \\ \frac{\partial z}{\partial s} &= \frac{\xi_3}{n}, & \frac{\partial \xi_3}{\partial s} &= \frac{\partial n}{\partial z} \end{aligned} \tag{20}$$

The ODE system resulting from the Eikonal equation (20) is solved in each step using a fourth order Runge-Kutta method (RK4). For a given ray, initial conditions are prescribed in terms of position and angle:

$$\begin{aligned} x(s)|_{s=0} &= x_0, \qquad \xi_1(s)|_{s=0} = cos(\theta_0)cos(\alpha_0) \\ y(s)|_{s=0} &= y_0, \qquad \xi_2(s)|_{s=0} = cos(\theta_0)sin(\alpha_0) \\ z(s)|_{s=0} &= z_0, \qquad \xi_3(s)|_{s=0} = sin(\theta_0) \end{aligned} \tag{21}$$

where the angle α_0 is the angle on the plane x-y, and the angle θ_0 is the azimuthal angle with respect to the positive z axis. For the 3D formulation, the refractive index $\mu(x, y, z)$ gradient follows the 2D first order reconstruction. With the assumption of piece-wise planar function over the computational domain, the refractive index can be expressed as:

$$\mu\,(x, y, z) = \frac{\partial \mu}{\partial x}x + \frac{\partial \mu}{\partial y}y + \frac{\partial \mu}{\partial z}z + \mu_0 \tag{22}$$

For each mesh element, the gradient is computed by solving the following system of equation:

$$\begin{bmatrix} x_1 & y_1 & z_1 & 1 \\ x_2 & y_2 & z_2 & 1 \\ x_3 & y_3 & z_3 & 1 \end{bmatrix} \begin{bmatrix} \frac{\partial \mu}{\partial x} \\ \frac{\partial \mu}{\partial y} \\ \frac{\partial \mu}{\partial z} \\ \mu\,(x, y, z) \end{bmatrix} = \begin{bmatrix} \mu(x_1, y_1, z_1) \\ \mu(x_2, y_2, z_2) \\ \mu(x_3, y_3, z_3) \end{bmatrix} \tag{23}$$

where:

$$\nabla\mu|_{_{Th}} = \begin{bmatrix} \frac{\partial \mu}{\partial x} & \frac{\partial \mu}{\partial y} & \frac{\partial \mu}{\partial z} \end{bmatrix} \tag{24}$$

The nodal partial derivatives are the weighted sum of each of the partial derivatives of the elements associated with that node. The weightings $\omega_i = V_i/V_{tot}$ are the volumes of each 3D mesh element divided by the total volume of all elements associated with the specific node.

$$\nabla\mu|_{_n} = \sum_{i=1}^{k} \omega_i \nabla\mu|_{T_i} \tag{25}$$

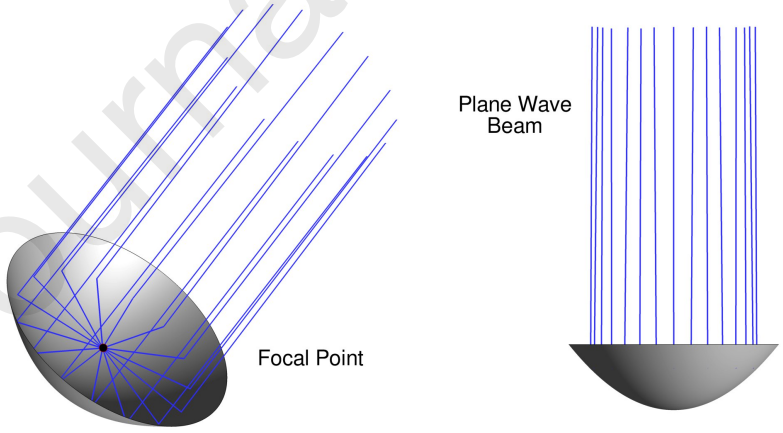

Figure 11: 3D reflection test: parabolic reflector.

Ray trajectories are verified with the 3D versions of the Luneburg and Maxwell fisheye, as shown in figure 10. Rays integration is completed when either it emerges from the computational domain or if it impinges the vehicle surface. The vehicle outer surface is modelled as a metallic solid wall, assuming that the presence of heat shields

materials does not affect the refractive property of the body. Thus, a solid reflection boundary condition is imposed when a ray impinges on the vehicle surface. In this case, new initial conditions are imposed to the ray, that will be re-shoot from the intersection point. To verify the proper interaction between 3D rays and solid surfaces, a benchmark case of a parabolic reflector is shown in figure 11. A parabolic reflector is a system with the property of transforming a spherical wave, with center in the paraboloid focal point, to a planar wave. The results confirm this property, as shown in figure 11. Finally, the I/O capabilty of the BORAT solver is tested using the computational domain of the ExoMars Schiaparelli capsule. Figure 12 shows a simplified ray tracing integration from the antenna location in a non-ionised domain for the 2D and 3D cases.

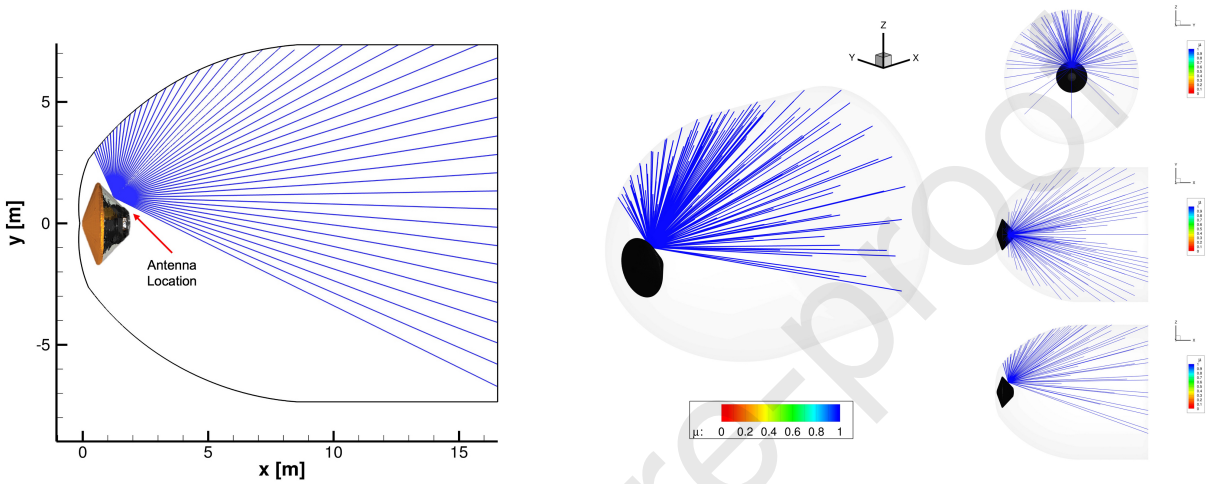

Figure 12: Ray tracing integration in non-ionised field: 2D domain (left) and 3D domain (right).

5. Numerical results

In this section the numerical simulations of the ExoMars atmospheric entry trajectory are presented. Figure 13 shows the computational domain used in this study. The ExoMars Schiaparelli geometry is a 71 degree sphere cone front shield with a nose radius of 0.06 m and an overall vehicle diameter of 2.4 m. A 0.06 m radius shoulder connects the forebody to a 47-deg conical back shield. ANSYS ICEM CFD Release 20.1® has been used to create a multiblock grid, which has been gradually coarsened towards the wake region and is orthogonal to the body at its surface. The computational domain extends 10 vehicles radii downstream to allow for an extended representation of the wake. To reduce the computational cost, the flow is assumed axial-symmetric which can be considered a valid assumption as the maximum angle of attack during entry is only 6 degrees over the entire trajectory. The free-stream conditions for the trajectory points which are investigated here are given in Table 1.

The flow field is further assumed to be steady and laminar, with a free-stream composition of 96% CO_2 and 4% N_2. The vehicle walls are assumed non-catalytic and iso-thermal, with temperature set to 1500 K. The flow is described as a single-fluid accounting for chemical non-equilibrium effects. The reference chemical model for the Martian atmosphere is the 18-species 33-reactions model proposed by [36]. As the maximum entry velocity of ExoMars Schiaparelli is below 5.9 km/s, a reduced mechanism is considered. This reduced mechanism, which is accurate enough to simulate the electron density for the conditions adopted here, is a 14-species mixture made of CO_2, CO, CO^+ NO, NO^+, N_2, O_2, O_2^+ , N, C, C^+, O, O^+, e, adapted from [36], where it was also shown that, for the velocity regime of this work, a single temperature could be used to account for non-equilibrium effects.

5.0.1. CFD simulations

In Figure 14, the computed electron number densities for the different trajectory points are compared against the critical electron density for the 400 MHz UHF antenna (horizontal red line). In the left plot, the electron density

Table 1: Free stream conditions of ExoMars Schiaparelli at different trajectory points.

Case	$t[s]$	$h[km]$	$\rho_\infty\ [kg/m^3]$	$V_\infty\ [m/s]$	$T_\infty\ [K]$	M_∞
a	22	96	6.97 x 10^{-6}	5867	165	28.4
b	27	91	1.29 x 10^{-5}	5859	155	29.3
c	38	80	3.72 x 10^{-5}	5856	175	27.5
d	50	71	1.10 x 10^{-4}	5736	168	27.4
e	62	63	2.90 x 10^{-4}	5269	169	25.1
f	73	56	5.82 x 10^{-4}	4516	174	21.2
g	77	54	7.13 x 10^{-4}	4192	177	19.5
h	80	52	8.25 x 10^{-4}	3941	180	18.2
i	85	50	1.01 x 10^{-3}	3532	184	16.1
j	92	48	1.27 x 10^{-6}	3006	189	13.6

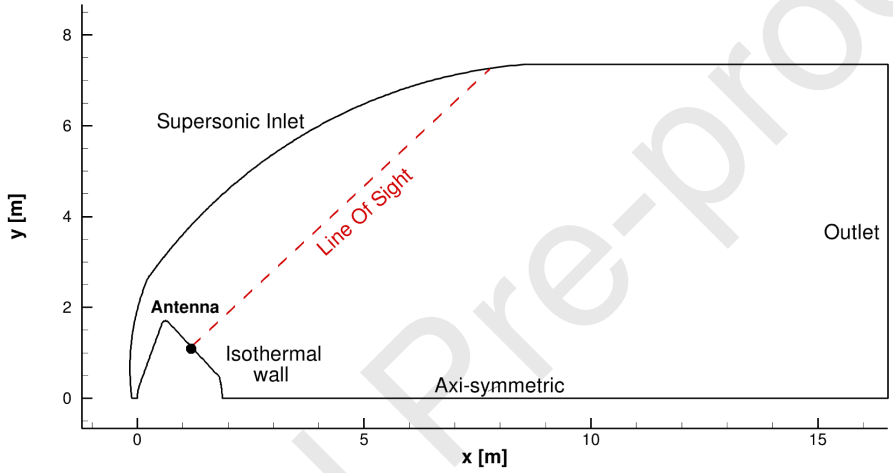

Figure 13: Computational domain with boundary conditions and antenna location.

distribution along the 40 degrees LOS between the on-board antenna and the receiving satellite is shown. On the right, the maximum electron density along the LOS is plotted for each trajectory point during the time of entry. A parabolic curve was fitted to the data to illustrate the general trend.

The comparison to the critical electron number density of the UHF transmission system shows that the peak of the blackout phase lies between 38 and 62 seconds, a period for which the ray tracing analysis shows that the shielding effect of the plasma is maximal.

At the end of the analysed trajectory phase (*h-i*), the computed electron number density is below the threshold of the critical electron number density. 3D effects (*e.g.*, angle of attack different from 0), and possibly turbulence should be taken into account to fully compute the terminal phase of the entry. However, despite the fact that the electron number density is lower than the critical electron density in this region, the ray tracing analysis still predicts disruption of the signal due to the plasma formation, as will be discussed in the next sections. Figures 15 and 16 show the different temperature and electron number density fields at (c) $h = 80\,\text{km}$ ($t = 38\,\text{s}$), 80 and 92 seconds during the atmospheric entry trajectory, with respectively a free-stream Mach number of 27, 18 and 13. The intent is for highlighting the main differences between the atmospheric entry flight regarding the blackout problem.

The main flow feature that characterizes the solutions is the strong shock generated in front of the spacecraft allowing the flow to decelerate and pass over the surface of the body. In this region high temperature peaks arise and the ionization levels of the flow reach their maximum. Subsequently, the flow is cooled down and accelerated over the vehicle shoulder by an expansion fan, that lowers the ionization levels of the flow. Generally, this is the region

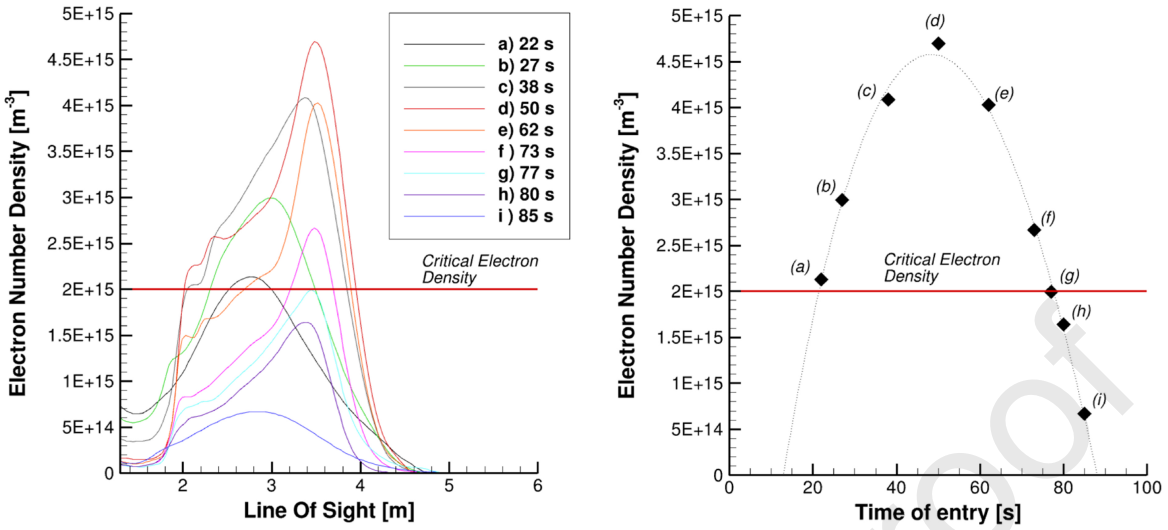

Figure 14: For each trajectory point : (left) electron number density distribution along LOS, (right) maximum electron number density along LOS.

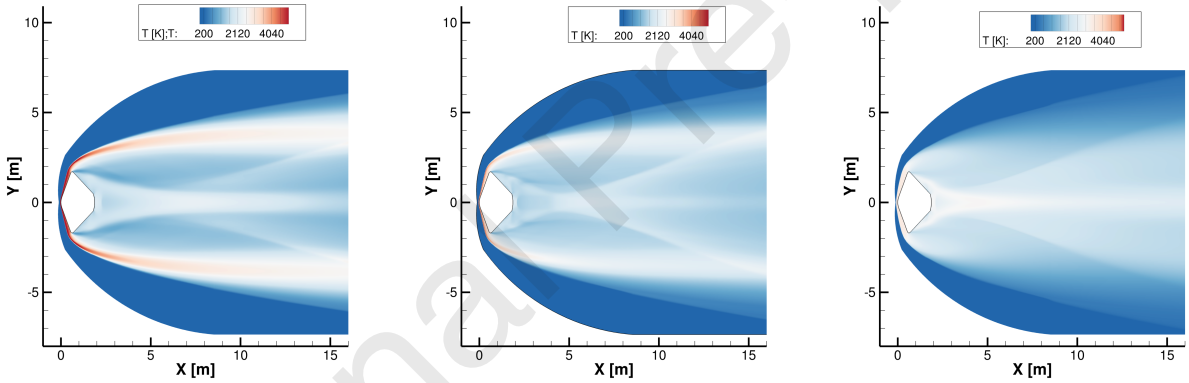

Figure 15: Temperature fields: (c) $h = 80$ km ($t = 38$ s) (left), (h) 52 km ($t = 80$ s) (center), (j) 48 km ($t = 92$ s) (right).

where spacecrafts mount communications antennas to partially overcome blackout conditions. The wake region is characterized by a recirculation region and a recompression zone, that increases electron densities in the wake. The refractive index is the parameter that describes the propagation of an EM wave in plasma, is computed and displayed for the selected ExoMars trajectory points in figure 17 for the ExoMars on-board antenna transmission frequency of $f = 400$Mhz. At 38s after the entry in the Martian atmosphere, the high velocity of the vehicle generates high temperature effects that leads to an high ionization of the flow. In all cases the refractive index approaches unity in the free-stream zones, at the side edges of the shock wave and in the central part of the wake. The 92s solution point belong to the terminal phase of the blackout period of the ExoMars capsule. Ionisation levels are low with respect to the critical electron number density of the emitting antenna frequency, thus the refractive index field is almost equal to 1 in the whole domain.

The numerical simulations presented in this work have been computed by the use of a chemical-nonequilibrium (CNEQ) model with the COOLFluiD CFD solver. To assess the validity of the thermal-equilibrium assumption for the ExoMars entry, two different calculations, with CNEQ and two-temperature thermochemical nonequilibrium

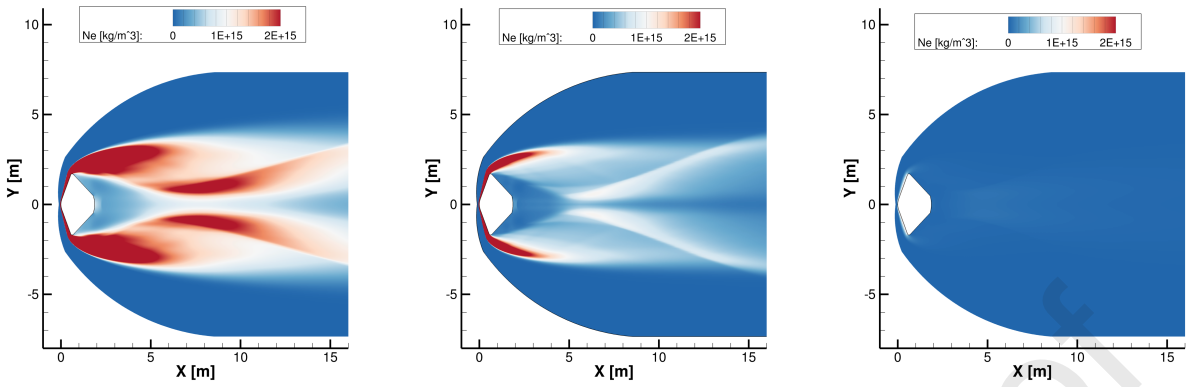

Figure 16: Electron Number Density N_e fields: (c) $h = 80$ km ($t = 38$ s) (left), (h) 52 km ($t = 80$ s) (center), (j) 48 km ($t = 92$ s) (right).

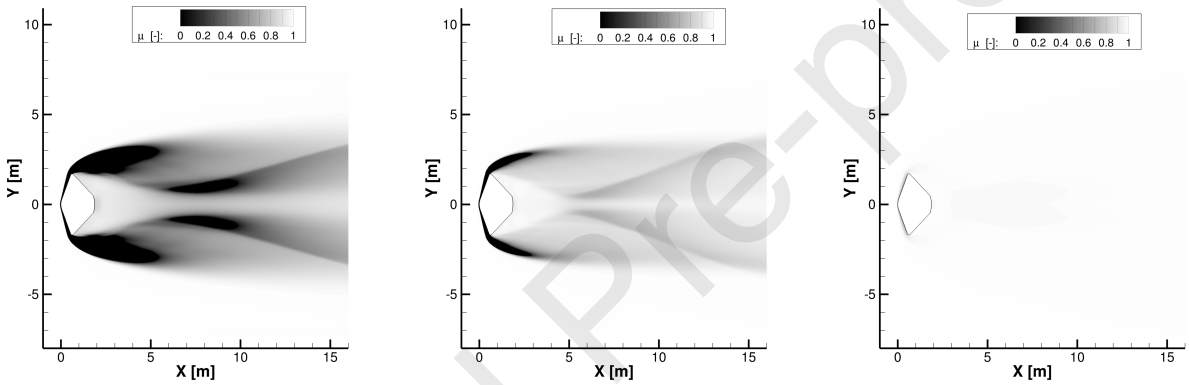

Figure 17: Refractive index μ fields:(c) $h = 80$ km ($t = 38$ s) (left), (h) 52 km ($t = 80$ s) (center), (j) 48 km ($t = 92$ s) (right).

(TCNEQ) models, have been computed and compared. The results of the two models are shown in Figure 18 for the trajectory point at 73 seconds after the start of the atmospheric entry, point (e) in Table 1. On the left, the comparison of refractive index fields for the CNEQ model (top) and TCNEQ (bottom). On the right, the comparison of electron density distribution along the LOS. The good agreement between the two models confirms the validity of the CNEQ assumption for the ray tracing analysis.

5.1. Ray Tracing Analysis 2D

The results of the coupled CFD simulations and ray tracing method are presented in this section. The ray tracing analysis has been performed over a 2D domain, considering the non-symmetrical position of the antenna and its influence on the EM propagation within the plasma. This has been obtained by mirroring the CFD solution with respect to the symmetry axis. The ExoMars Schiaparelli on-board antenna is modeled with an aperture of 70 degrees with respect to the normal to the body, with a transmission frequency of 400 MHz, located on the $+y$ lateral face of the vehicle body (as shown in Figure 13). Figures 19 shows the solution of the ray tracing analysis superposed to the gray scale refractive index contour plot for the trajectory points of Table 1.

The analysed trajectory points show the evolution of the blackout period from its onset at (*a*), to its peak (*b-e*), to the terminal brownout phases (*f-i*). The on board antenna signal is discretized with 600 rays, integrated until emerging from the entry plasma. The incoming flow accelerates over the shoulder of the capsule by forming an expansion fan, which cools down the flow and thus lowers the ionization levels of the flow. We observe in Fig. 19 that a

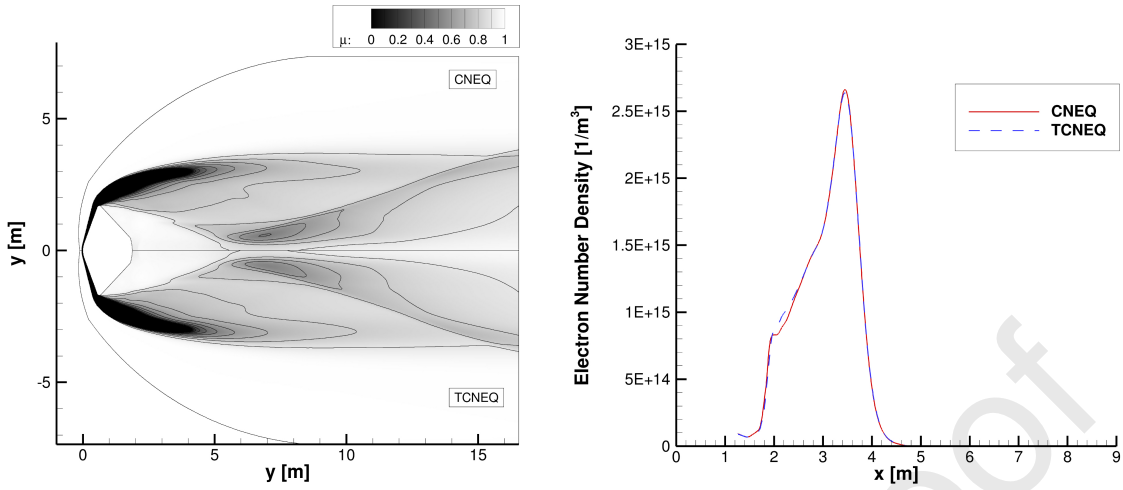

Figure 18: Comparison of CNEQ flow simulation and TCNEQ flow simulation for the entry trajectory point at (f) 56 km (t = 73 s) : refractive index field (left) and electron density distribution along LOS (right).

plasma region is formed around the ExoMars capsule whose strength can be correlated with the refractive index of the region. It is observed in the solutions that the low refractive index zones act as a reflecting surface for the EM waves, generating a shielding effect around the spacecraft. The ray colors are based on the refractive index values of the plasma field along the trajectory. This choice of representation allows to highlight the strong reflections of the rays, mostly occurring at the peak of the blackout phase (*c*-*d*) which is characterized by low values of the refractive index. Rays encounter strong reflections near the shoulder of the vehicle and a series of multiple refractions in the wake region. At maximum blackout conditions (*d*), the vast majority of the rays are converged in the wake and shielded by the plasma. Moreover, during this strong blackout phase, the wake is characterized by high electron number density that creates strong electromagnetic interference with the onboard instrumentation. The communications antennas are usually placed in the back shell of capsule to partially overcome blackout conditions. Using CFD and BORAT, we trace the behavior of communication signal rays emitted by one such antenna on the ExoMars capsule. A very high temperature of shock coupled with decelerating flow and an increasing atmospheric density result in a strong plasma sheath around the vehicle during 91 to 63 km altitude during its decent. During these altitudes, the flow around the capsule remains hotter relative to flight conditions at other altitudes and the signal emitted by the antenna is perpetually trapped in the plasma, as compared to other altitudes, resulting in total loss of communication for almost 35 seconds during its decent phase.

The brownout phases (*f*-*i*) are characterized by lower ionisation levels of the flow that result in less disruption of the electromagnetic wave signal. As the shock strength decreases during the brownout phases, the electron density decreases due to lower flow temperature, thus resulting in a region of lower electron density around the vehicle. In general, the entry plasma wraps the vehicle and forms a shielding cup around it. Because of the reflection at the plasma, the cup has a potential for focussing/defocussing the rays, a fact that may generate directive patterns in certain angular regions. During brownout, not all the EM waves are fully encapsulated in the plasma layer. In this condition, the presence of plasma redirects the rays, creating communication windows that could possibly be used as alternative communication paths. Using BORAT, we observe that at these flight conditions (e.g. in Fig. 19 (*a*) and from Fig. 19 (*f*-*i*)) the rays are able to escape the plasma sheath and thus result in continuous communication with the capsule at those altitude. We observe that the flow physics needs to be modeled accurately, since even when a plasma is present in the front of the vehicle, continuous communication can be achieved. Moreover, BORAT can help to precisely predict communication blackout during the descent phase. It can also assist in optimal placement of the communication antenna during entry and help in quantifying the different blackout mitigation strategies that can be employed to further minimize communication blackout.

A different way to analyse the effect of the presence of plasma on the communication system is the use of radiation patterns. Radiation patterns are commonly used to show aperture angles and signal strength of antennas. In this paper

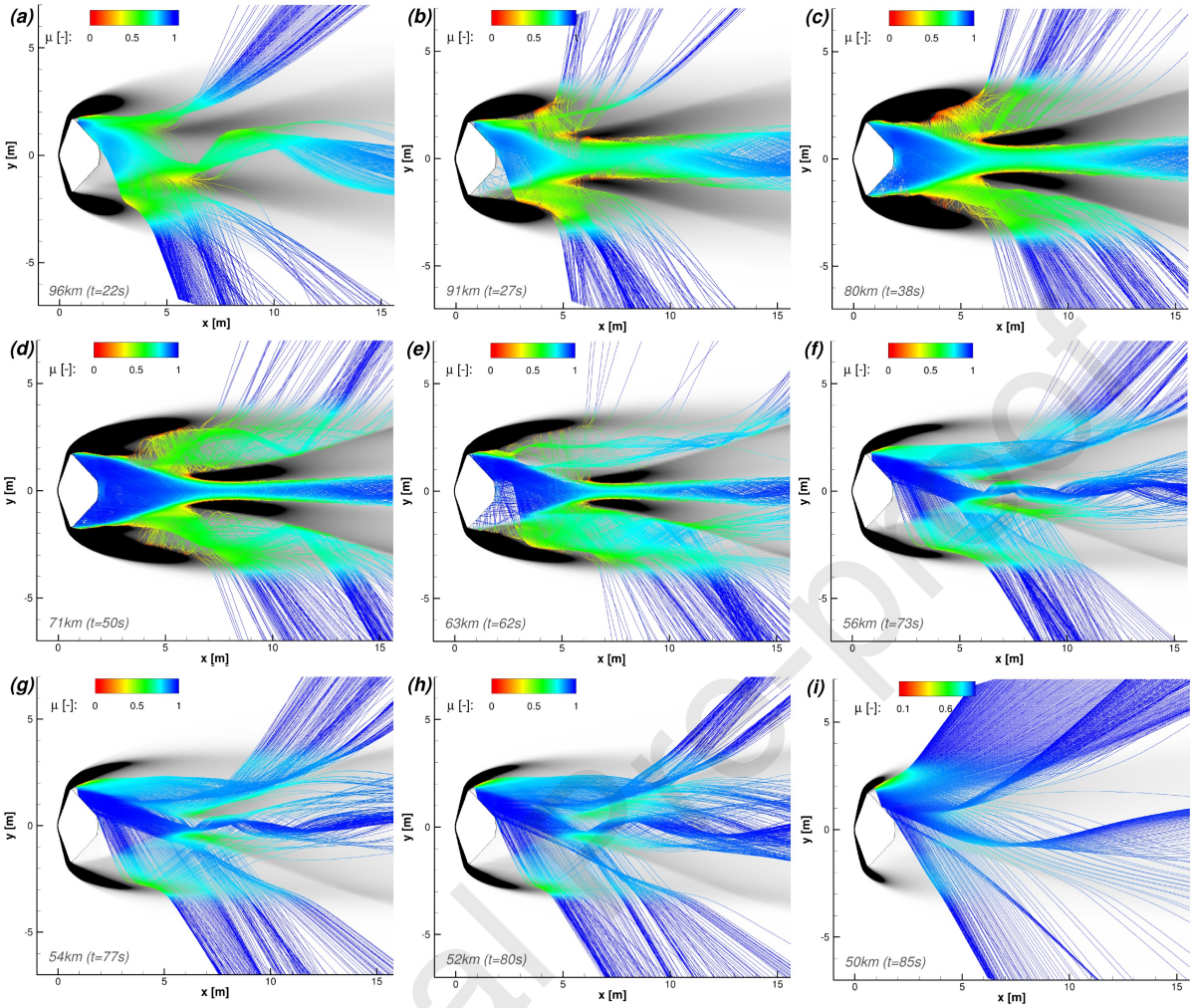

Figure 19: Ray tracing solution during ExoMars atmospheric entry at: (a) 96 km (t = 22 s), (b) h = 91 km (t = 27 s), (c) h = 80 km (t = 38 s), (d) h = 71 km (t = 50 s), (e) 63 km (t = 62 s), (f) 56 km (t = 73 s), (g) 54 km (t = 77 s), (h) 52 km (t = 80 s), (i) 50 km (t = 85 s).

a simplified approach consisting in the application of the antenna power conservation is considered. Any dissipation of the emitted EM signal due to the interaction with plasma will be assessed in future work. With this simplification, the angular power density $U_i(s)$ emitted by the on-board antenna, that is conserved through rays integration, is calculated using the following equation [15]:

$$U_i(s) = \frac{P_{antenna}}{2\pi} g \frac{\Delta\theta(0)}{\Delta\theta_i(s)} \tag{26}$$

where $P_{antenna}$ is the power emitted by the antenna, g is the antenna gain, $\Delta\theta(0)$ the angle between two adjacent rays (n and $n+1$) at initial conditions and $\Delta\theta_i(s)$ the angle at position s between the ray n and $n+1$. The antenna is assumed ideal with an uniform radiation over the aperture angle and an antenna gain of 1. The calculated power density is then converted into dB. Figure 20 shows the ideal radiation patterns at different trajectory points over the ExoMars entry. Each solution is over-imposed on the free space solution, which is calculated as the radiation pattern with no plasma generation within the flow. It can be seen how the presence of plasma generates shadow zones that shields the spacecraft from communications. Peaks in the signal strength are due to the focusing of rays in a specific direction, while an aperture angle increase results in a signal strength decreased. The ideal signal strength over the

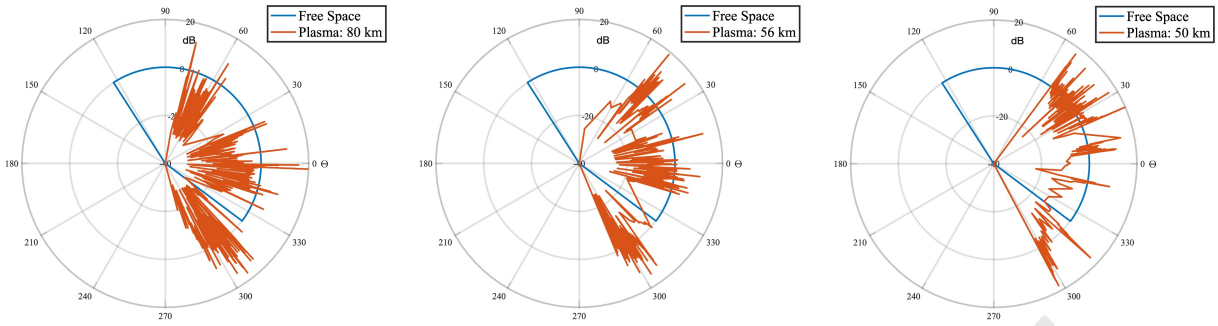

Figure 20: Radiation patterns of ExoMars UHF antenna at (c) $h = 80\,\text{km}$ ($t = 38\,\text{s}$) (left), (f) $h = 56\,\text{km}$ ($t = 73\,\text{s}$) (center) and (i) $h = 50\,\text{km}$ ($t = 85\,\text{s}$) (right).

increased radiation angle has decreased as expected and fits very well to the ray densities escaping in those directions. In general, the radiation patterns shows that a certain ray density is required to have a wider effective radiation pattern. If single rays are too much apart from each other they do not radiate enough power to be visible in the radiation pattern.

5.2. Ray Tracing Analysis 3D

This section presents a 3D analysis of the EM waves propagation for the ExoMars entry by the use of the newly developed BORAT 3.0 solver. Due to the low angle of attack flight conditions of the ExoMars atmospheric entry phase, in first approximation the 2D axisymmetric CFD solution can be considered representative of the a fully 3D CFD computation. Future work will focus on 3D CFD computations with angles of attack different from zero to reproduce real flight configurations. To generate a 3D CFD solution input for the ray tracing solver, the 2D solutions have been interpolated on a 3D mesh. Figure 21 shows the intermediate steps of the procedure, that starts with the generation of rotational planes from the original 2D mesh, sampled at 1 degree to generate a dense spatial distribution. Then the rotational planes point distribution are used to interpolate the CFD nodal solution via use of inverse distance interpolation. The 3D reconstructed solution is based on 6 million cells unstructured tetrahedral mesh, which has been generated with the ANSYS Gambit mesh generation software. Number of rational planes, size quality and distribution of the 3D mesh have been selected to reduce to the minimum the noise induced by the interpolation procedure, as confirmed in figure22. Considering the zero-angle of attack entry configuration, the results are in line with the 2D analysis if compared on the z-y symmetry plane, as visible in figure 22, which shows a comparison between the 2D and the 3D ray tracing solution at two trajectory points (c,f).

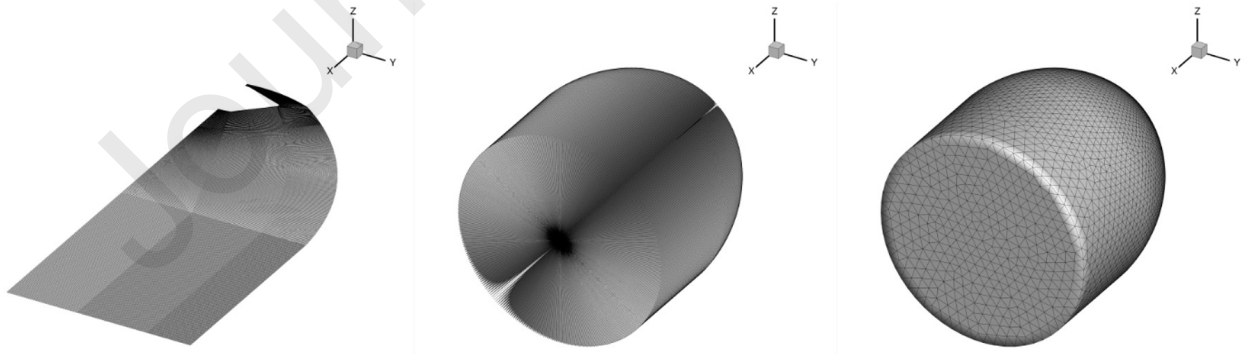

Figure 21: ExoMars solution reconstruction with 3D interpolation from 2D axisymmetric solution.

After the generation of the 3D input solution files via interpolation, the ray tracing analysis has been conducted for the entry trajectory points in Table 1. In 3D configuration, the emitting antenna is located on the z-x symmetry plane,

at the same location of the 2D analysis. The antenna signal is modelled with an omnidirectional beam of 180 rays with a 70 degrees cone aperture with respect the normal to the spacecraft. For each solution two different iso-surfaces are highlighted: the first iso-surface (darker in colour and close to the spacecraft body) is the μ=0 surface, delimiting the zones at high ionisation generated during the blackout and shielding the emitted signal from the propagation in the plasma layer. The iso-surface at $\mu = 1$ delimits the bow shock surface from which the plasma layer is generated around the spacecraft. All rays are coloured depending on the refractive index value of the field encountered in their path.

Figure 24 shows the 3D ray tracing solutions for the ExoMars, assuming a zero-angle of attack entry, between 96 and 50 km. The 3D visualization highlights the main favourable direction of communication during the entry trajectory. Side views on vertical planes are also presented for each plot, highlighting the presence of out of plane propagations. Generally, at the onset and end of the blackout phase it is not likely that all EM waves are fully contained within the plasma layer. Reflections and refractions of the emitted EM waves are the leading phenomena of these entry phases, and their effect must be taken into account. The use of ray tracing allows for gathering information on possible alternative communication directions during these flight phases, since the accurate EM waves path can be fully reproduced with this method. This analysis is extremely important for both characterizing accurately enough the blackout physical phenomena and to gather important information for possible mitigation solutions. Additionally, 3D effects and out of plane propagation must be taken into account in order to perform accurate blackout prediction, considering the intrinsically asymmetric nature of real flight configurations.

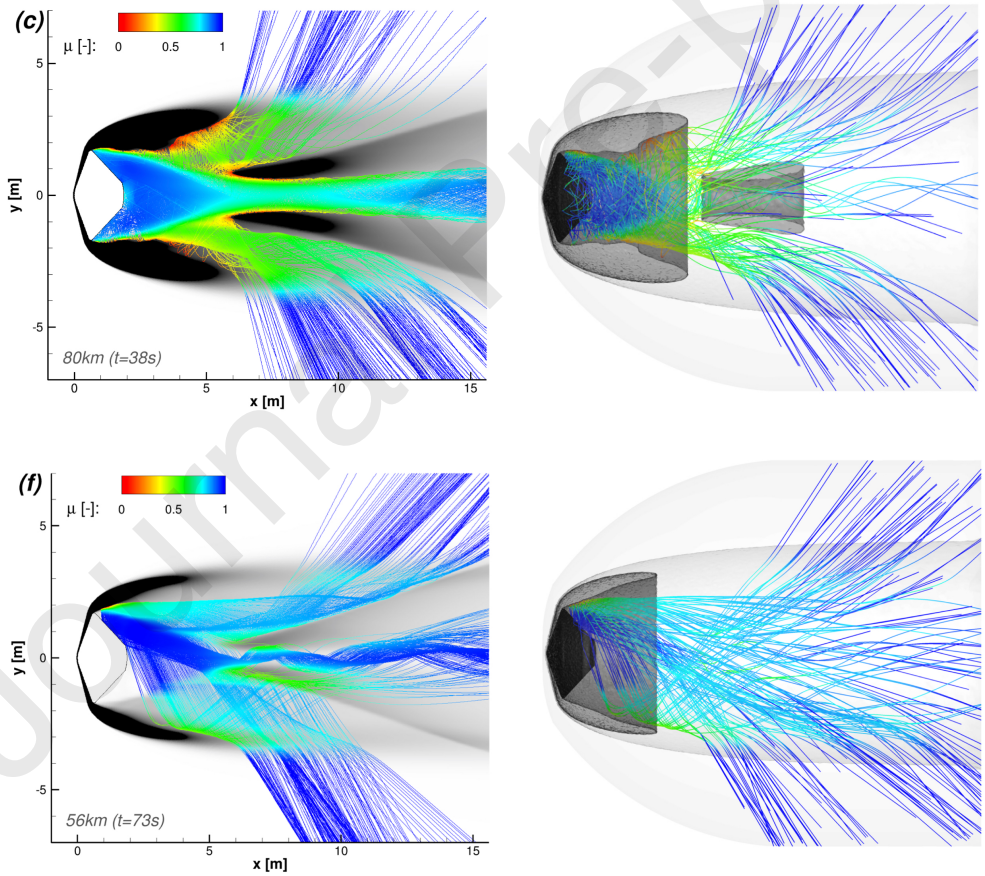

Figure 22: Comparison of 2D ray tracing solution with 3D ray tracing solution: x-y plane view. Left, 2D solutions, right, 3D solution.

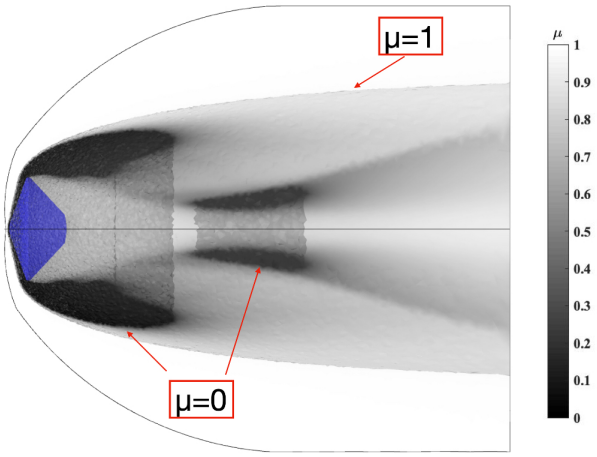

Figure 23: Iso-surfaces definition for 3D ray tracing visualization: x-y plane view.

6. Conclusion

This paper presents the development and application of a 3D ray tracing method for the analysis of communication blackout during space (re-)entry flight conditions. To this end, the existing BORAT code, originally using the Snell's law as marching-in-space method to calculate the ray propagation in 2D, has been further extended by implementing a new solver using the Eikonal equations to calculate the ray path in 2D and 3D. Both Eikonal solvers have been verified on benchmark cases with known solutions in order to check the consistency of their implementation. As a result, the BORAT-based numerical software for analysing/predicting blackout conditions has been upgraded to a 3D formulation in order to deliver a tool capable of reproducing real flight configurations. The blackout analysis has been based on the application of CFD simulations, performed with the COOLFluiD CNEQ solver (using the PLATO library for computing non-equilibrium plasma properties) in combination with BORAT (version 3.0). The developed methodology has been applied to analyse a real-case scenario, i.e. the ESA 2016 ExoMars Schiaparelli mission. Numerical CFD simulation have been performed at different entry trajectory points, assuming chemical non-equilibrium and thermal equilibrium for a 14-species Martian atmosphere mixture, assuming a zero-angle of attack flight configuration. The numerical results confirm that radio blackout is mostly due to encapsulation of rays by the plasma rather than absorption of the signal. Furthermore, reflection and refraction phenomena can make RF signal rays escape the entry plasma layer. Advanced analysis methods, such as the one presented in this work, allows for properly predicting the emitted signal path in the plasma flow, thus gathering more information on possible alternative communication directions during blackout. This is extremely important for the brownout phases, where, due to lower ionization levels of the flow, the emitted radio waves can possibly reach the receiving spacecraft through refraction and reflection. Moreover, BORAT can help to precisely predict communication blackout during the decent phase. It can also assist in optimal placement of the communication antenna during decent and help in quantifying the different blackout mitigation strategies that can be employed to further minimize communication blackout.

Acknowledgments

The research of Vincent Fitzgerald Giangaspero is supported by SB PhD fellowship 1SA8219N of the the Research Foundation - Flanders (FWO).

The resources and services used in this work were provided by the VSC (Flemish Supercomputer Center), funded by the Research Foundation - Flanders (FWO) and the Flemish Government.

This project has received funding from the European Union's Horizon 2020 Research and Innovation Program under grant agreement 899298 (MHD-Enabled Entry Systems for Space Transportation, aka MEESST). This paper

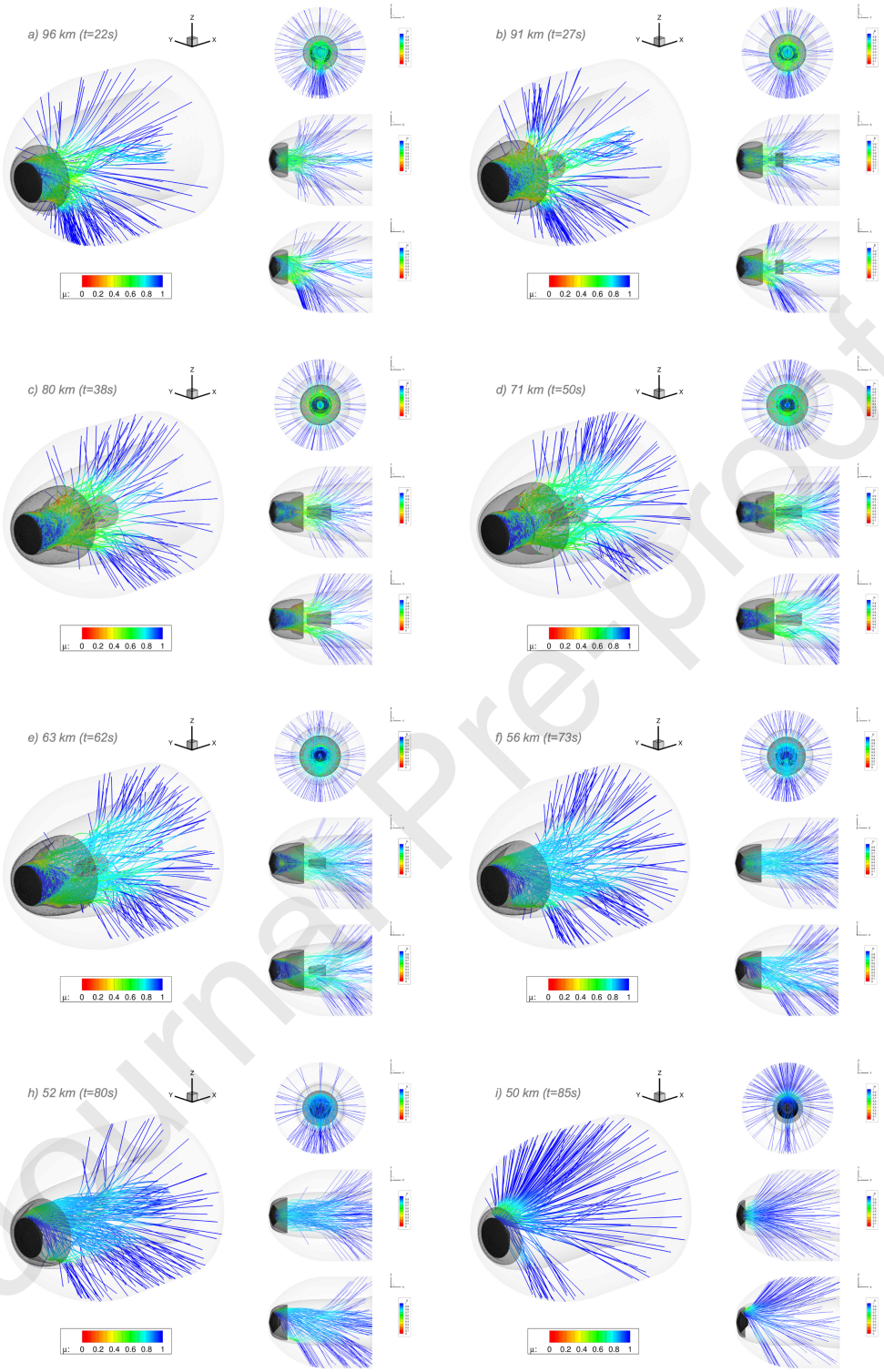

Figure 24: 3D ray tracing solution during ExoMars atmospheric entry at (a) 96 km (t = 22 s), (b) h = 91 km (t = 27 s), (c) h = 80 km (t = 38 s), (d) h = 71 km (t = 50 s), (e) 63 km (t = 62 s), (f) 56 km (t = 73 s), (h) 52 km (t = 80 s), (i) 50 km (t = 85 s).

reflects only the authors'view, and the European Commission is not responsible for any use that may be made of the information it contains.

Appendix. Implementation of BORAT solver

This appendix shows a concise overview about the implementation of the BORAT ray tracing solver.

```
Data: Set of mesh cells, Ray solutions
Input: flowfieldfilename, antenna
Output: solution_file, rays_solution
initialization;
domain ← readflowfield_tecplot(flowfieldfilename) ;
nNodes ← number of nodes in input mesh ;
for i ← 1 to nNodes do
    nodeState ←opticalProperties ;
    nodeState ←gradients ;
if solverSnell == true then
    rays_solution.solver ← solver_SnellLaw;
else
    if solverEikonal == true then
        rays_solution.solver ← solver_Eikonal;
nRay ← number of ray for antenna discretization ;
for i ← 1 to nRay do
    rays_solution.XYZ[i] ← initialization antenna position ;
    rays_solution.UVW[i] ← initialization shooting angle ;
    isInside ← true ;
    while isInside == true do
        rays_solution.XYZ[i], rays_solution.UVW[i] ← integration step;
        if isInside ≠ true then
            if isBoundaryReflection == true then
                rays_solution.[i] ← reflection ++;
                rays_solution.XYZ[i] ← re-initialization with reflection rays_solution.UVW[i] ←
                  re-initialization with reflection ;
                isInside ← true ;
            else
                rays_solution.[i] ← end of integration for ray i
draw_raytracing_solution(rays_solution) ;
save_solutionfile(solution_file) ;
export_raytracing_tecplot(solution_file) ;
```

Algorithm 1: BORAT main

References

[1] Y. Takahashi, T. Koike, N. Oshima, K. Yamada, Aerothermodynamic analysis for deformed membrane of inflatable aeroshell in orbital reentry mission, Aerospace Science and Technology 92 (2019) 858–868.

[2] K. Minkwan, M. Keidar, I. D. Boyd, Analysis of an electromagnetic mitigation scheme for reentry telemetry through plasma, Journal of Spacecraft and Rockets 45 (6) (2008) 1223–1229.

[3] E. Bögel, M. A. La Rosa Betancourt, M. R. Collier-Wright, Magnetohydrodynamic enhanced entry system for space transportation (meesst) as a key building block for future exploration missions, in: AIAA Propulsion and Energy 2021 Forum, 2021, p. 3272.

[4] S. Portigliotti, C. Cassi, M. Montagna, P. Martella, M. Faletra, J. Boi, S. De Sanctis, D. Granà, O. Bayle, T. Blancquaert, et al., Exomars 2016, the schiaparelli mission. edl demonstration results from real time telemetry before unfortunate impact, in: 14th International Planetary Probe Workshop, 2017.

[5] T. Tolker-Nielsen, Exomars 2016-schiaparelli anomaly inquiry (2017).

[6] A. Viviani, A. Aprovitola, L. Iuspa, G. Pezzella, Aeroshape design of reusable re-entry vehicles by multidisciplinary optimization and computational fluid dynamics, Aerospace Science and Technology 105 (2020) 106029.

[7] M. Kim, Active plasma layer manipulation scheme during hypersonic flight, Aerospace Science and Technology 35 (2014) 135–142.

[8] I. Boyd, Modeling of plasma formation in rarefied hypersonic entry flows, in: 45th AIAA Aerospace Sciences Meeting and Exhibit, 2007, p. 206.

[9] D. Morabito, R. Kornfeld, K. Bruvold, L. Craig, K. Edquist, The mars phoenix communications brownout during entry into the martian atmosphere, The Interplanetary Network Progress Report 42 (2009) 179.

[10] H. Zhou, X. Li, K. Xie, Y. Liu, Y. Yu, Mitigating reentry radio blackout by using a traveling magnetic field, Aip Advances 7 (10) (2017) 105314.

[11] M. Kundrapu, J. Loverich, K. Beckwith, P. Stoltz, A. Shashurin, M. Keidar, Electromagnetic wave propagation in the plasma layer of a reentry vehicle, in: 2014 IEEE 41st International Conference on Plasma Sciences (ICOPS) held with 2014 IEEE International Conference on High-Power Particle Beams (BEAMS), IEEE, 2014, pp. 1–4.

[12] Y. Takahashi, R. Nakasato, N. Oshima, Analysis of radio frequency blackout for a blunt-body capsule in atmospheric reentry missions, Aerospace 3 (1) (2016) 2.

[13] S. Ramjatan, T. Magin, T. Scholz, V. Van der Haegen, J. Thoemel, Blackout analysis of small cone-shaped reentry vehicles, Journal of Thermophysics and Heat Transfer 31 (2) (2017) 269–282.

[14] Y. Takahashi, K. Yamada, T. Abe, Prediction performance of blackout and plasma attenuation in atmospheric reentry demonstrator mission, Journal of Spacecraft and Rockets 51 (6) (2014) 1954–1964.

[15] C. Vecchi, M. Sabbadini, R. Maggiora, A. Siciliano, Modelling of antenna radiation pattern of a re-entry vehicle in presence of plasma, in: IEEE Antennas and Propagation Society Symposium, 2004., Vol. 1, IEEE, 2004, pp. 181–184.

[16] D. Morabito, B. Schratz, K. Bruvold, P. Ilott, K. Edquist, A. D. Cianciolo, The mars science laboratory edl communications brownout and blackout at uhf, Interplanetary Network Progress Report 197 (27) (2014) 1–22.

[17] S. Ramjatan, A. Lani, S. Boccelli, B. Van Hove, Ö. Karatekin, T. Magin, J. Thoemel, Blackout analysis of mars entry missions, Journal of Fluid Mechanics 904 (2020).

[18] V. F. Giangaspero, A. Lani, S. Poedts, J. Thoemel, A. Munafò, Radio communication blackout analysis of exomars re-entry mission using raytracing method, in: AIAA Scitech 2021 Forum, 2021, p. 0154.

[19] H. Ling, R.-C. Chou, S.-W. Lee, Shooting and bouncing rays: Calculating the rcs of an arbitrarily shaped cavity, IEEE Transactions on Antennas and propagation 37 (2) (1989) 194–205.

[20] A. Lani, T. Quintino, D. Kimpe, H. Deconinck, S. Vandewalle, S. Poedts, The coolfluid framework: design solutions for high performance object oriented scientific computing software, in: International Conference on Computational Science, Springer, 2005, pp. 279–286.

[21] A. Lani, An object oriented and high performance platform for aerothermodynamics simulation, Université Libre de Bruxelles (2008).

[22] A. Lani, N. Villedie, K. Bensassi, L. Koloszar, M. Vymazal, S. Yalim, M. Panesi, Coolfluid: an open computational platform for multi-physics simulation and research, in: 21st AIAA Computational Fluid Dynamics Conference, 2013, p. 2589.

[23] S. Balay, S. Abhyankar, M. F. Adams, S. Benson, J. Brown, P. Brune, K. Buschelman, E. M. Constantinescu, L. Dalcin, A. Dener, V. Eijkhout, W. D. Gropp, V. Hapla, T. Isaac, P. Jolivet, D. Karpeev, D. Kaushik, M. G. Knepley, F. Kong, S. Kruger, D. A. May, L. C. McInnes, R. T. Mills, L. Mitchell, T. Munson, J. E. Roman, K. Rupp, P. Sanan, J. Sarich, B. F. Smith, S. Zampini, H. Zhang, H. Zhang, J. Zhang, PETSc Web page, `https://petsc.org/` (2022).
URL `https://petsc.org/`

[24] A. Alberti, A. Munafò, M. Koll, M. Nishihara, C. Pantano, J. Freund, G. Elliott, M. Panesi, Laser-induced non-equilibrium plasma kernel dynamics, Journal of Physics D: Applied Physics 53 (2) (2019) 025201.

[25] A. Munafò, A. Alberti, C. Pantano, M. Freund, J.B. Panesi, A computational model for nanosecond pulse laser-plasma interactions, J. Comput. Phys. 406 (2020) 109190.

[26] A. A. Laguna, N. Ozak, A. Lani, H. Deconinck, S. Poedts, Fully-implicit finite volume method for the ideal two-fluid plasma model, Computer Physics Communications 231 (2018) 31–44.

[27] G. Degrez, A. Lani, M. Panesi, O. Chazot, H. Deconinck, Modelling of high-enthalpy, high-mach number flows, Journal of Physics D: Applied Physics 42 (19) (2009) 194004.

[28] K. Bensassi, A. Lani, P. Rambaud, Unsteady simulation of hypersonic flow around a heat flux probe in ground testing conditions, International Journal of Heat and Mass Transfer 113 (2017) 889–897.

[29] D. Knight, J. Longo, D. Drikakis, D. Gaitonde, A. Lani, I. Nompelis, B. Reimann, L. Walpot, Assessment of cfd capability for prediction of hypersonic shock interactions, Progress in Aerospace Sciences 48 (2012) 8–26.

[30] K. G. Budden, Radio waves in the ionosphere, Radio Waves in the Ionosphere (2009).

[31] K. Davies, Ionospheric radio propagation, Vol. 80, US Department of Commerce, National Bureau of Standards, 1965.

[32] Y. A. Kravtsov, Y. I. Orlov, Geometrical optics of inhomogeneous media, Vol. 38, Springer, 1990.

[33] J. R. Dormand, P. J. Prince, A family of embedded runge-kutta formulae, Journal of computational and applied mathematics 6 (1) (1980) 19–26.

[34] R. K. Luneburg, Mathematical theory of optics, University of California press, 1964.

[35] W. Whewell, The Cambridge and Dublin Mathematical Journal, no. v. 9 in Landmarks II: Journals, E. Johnson, 1854.
URL `https://books.google.be/books?id=-bI5AAAAMAAJ`

[36] C. Park, J. Howe, R. Jaffe, G. Candler, Review of chemical-kinetic problems of future nasa missions. ii-mars entries, Journal of Thermophysics and Heat transfer 8 (1) (1994) 9–23.

Declaration of interests

☒ The authors declare that they have no known competing financial interests or personal relationships that could have appeared to influence the work reported in this paper.

☐ The authors declare the following financial interests/personal relationships which may be considered as potential competing interests: